Master's thesis

NTNU
Norwegian University of Science and Technology
Faculty of Engineering
Department of Energy and Process Engineering

Frode Østby

Internal Temperature measurement in Lithium ion battery with FBG sensors

Master's thesis in Industrial Process Engineering
Supervisor: Jacob Joseph Lamb
Co-supervisor: Markus Solberg Whal, Lena Spitthoff
June 2021

NTNU
Kunnskap for en bedre verden

Frode Østby

Internal Temperature measurement in Lithium ion battery with FBG sensors

Master's thesis in Industrial Process Engineering
Supervisor: Jacob Joseph Lamb
Co-supervisor: Markus Solberg Whal, Lena Spitthoff
June 2021

Norwegian University of Science and Technology
Faculty of Engineering
Department of Energy and Process Engineering

NTNU
Norwegian University of
Science and Technology

Summary

In this thesis FBG sensors have been implemented into pre-fabricated LIBs for the purpose of measuring the internal temperature. Glass capillaries was used to isolate the sensors from strain contributions. To protect the capillaries at the entry point, a polypropylene bracket was used. The impact on the cell performance due to the sensor implementation was evaluated by examining change in capacity and internal resistance. Furthermore, temperature measurements was made during cycling of the cell to evaluate the performance of the sensors. It was found that the bracket protected the capillaries at the entry point of the cell as designed. However, due to the distortion of the cell pouch during vacuum sealing the capillaries had a tendency to break inside the cell. It was attempted to correct this by reducing the vacuum in the sealing process, but this lead to an insufficient seal and cell moisture ingress was present. Information about the cell electrolyte was also not available, which resulted in an unfavorable composition of the refilled electrolyte solvent. This made it difficult to determine whether the reduction in capacity of 10% and increase of internal resistance of 17% and 7% at 20% SOC and 40% SOC respectively was due to the change in electrolyte composition or the presence of sensors inside the cell. The temperature measurement showed expected values of 2.75℃ difference between internal and external sensors at 2 C discharge, indicating that the capillaries successfully eliminated any strain contributions. Furthermore, the observed temperature gradients demonstrate the value of internal measurements in LIBs.

Sammendrag

I denne masteroppgaven har det blitt implementert FBG-sensorer i forhåndsproduserte lithium-ion batterier for intern temperaturmåling. Det ble brukt glasskapillærer for å isolere sensorene slik at de kun regaerte på temperatur endringer. For å beskytte kapillærene ved inngangspunktet til cellen, ble det brukt en polypropylenbrakett. Effekten som sensorimplementeringen hadde på celleytelsen ble evaluert ved å undersøke endringer i kapasitet og intern motstand. Videre ble det foretatt temperaturmålinger under sykling av cellen for å evaluere ytelsen til sensorene. Det ble funnet at braketten beskyttet kapillærene ved inngangspunktet til cellen som designet. Men på grunn av forvrengning av celleposen under vakuumforsegling hadde kapillærene imidlertid en tendens til å knekke inne i cellen. Det ble forsøkt å korrigere dette ved å redusere vakuumet i forseglingsprosessen, men dette førte til utilstrekkelig forsegling og inntrenging av fuktighet i cellen. Informasjon om celleelektrolytten var ikke tilgjengelig, noe som resulterte i en mindre optimal sammensetning av det etterfylte elektrolyttløsningsmidlet. Dette gjorde det vanskelig å avgjøre om 10% reduksjonen i kapasitet og økning på 7 til 17% av intern motstand skyldtes endring i elektrolyttsammensetning eller tilstedeværelsen av sensorer inne i cellen. Temperaturmålingen viste forventede verdier med en maksimal forskjell på 2.75 C mellom interne og eksterne senorer, noe som indikerte at kapillærene tilstrekelig isolterte sensorene fra andre bidrag en temperatur. Videre underbygger de observerte temperaturgradientene verdien av interne målinger i lithium-ion batterier.

Table of content

List of Figures

List of Tables

1 Introduction

In the effort to cut global carbon emissions and combat climate change, there has been a rapid growth in renewable electricity production. This has created a need for more auxiliary energy storage for the purpose of peak shaving and grid stabilisation due to the intermittent nature of energy sources such as wind and solar power. In addition, the use of electrochemical energy storage for transport have been rapidly growing for the same reason, lower emissions than fossil based propulsion. Lithium ion batteries (LIB) are a widely utilized electrochemical energy storage technology for both stationary and mobile use due to the high energy and power density and low self discharge rate [5]. However, further electrification of our society is necessary to reach the 1.5°C goal, as fossil based electricity production and transport account for 45% of world wide carbon emissions [6]. For this to be realised, the performance of LIB systems must become as cost-efficient, safe and practical as fossil-based energy storage.

LIBs are versatile energy storage units that can store electrical energy as chemical energy, then readily discharge the energy potential as electricity. However, LIBs have application limitations, mainly due to production cost and lifetime expectancy. As different applications require different configurations and designs of LIB systems, current delivery, voltage and heat generation is affected. For high power applications this raises a set of challenges. Firstly, in transport, range is the main limiting factor. Reducing charging time can reduce the range limitations. However, high current densities generate more heat, and as battery lifetime is heavily dependent on operating temperature, fast charging requires a good understanding of the aging mechanisms involved. Effective, non restricting battery management systems (BMS) combined with adequate cooling systems is necessary for safe and effective operation [7]. Secondly, in stationary systems, either for off-grid supply or grid stabilisation, system cost is a challenge. For the cost of such systems to be acceptable, maximum lifetime and a high number of full equivalent cycles are necessary [8], which again rely on aging and BMS. Thirdly, in addition to cost related lifetime requirements, the lifetime of LIBs needs to be extended to the fullest to keep the carbon footprint low, as the production of LIBs are energy intensive and the LIBs are currently mainly produced in countries which use fossil based electricity for production. Finally, LIB safety is a limitation, where abusive conditions can lead to fire or explosion due to the phenomenon called thermal runaway. A better understanding of internal heat production and more accurate BMS can aid in preventing and possibly predict thermal runaway scenarios. Therefore, better Knowledge about internal temperature profiles and more accurate BMS are necessary. Elevating BMS performance can result in higher and safer systems performance, and knowledge about internal temperature profiles can increase knowledge on aging characteristics and possibly result in better battery design.

As illustrated in Fig. 1, BMS relies on measuring voltage, current and external temperature of the battery pack combined with models to estimate the parameters state of charge (SOC), State of health (SOH), cell resistance, cell capacities and internal temperature. This leads to conservative management due to uncertainty in the esti-

mated values [9]. Similarly, in battery research, internal states are estimated based on external measurements and modeling. Placing sensors at internal high value locations can increase the estimation accuracy for internal parameters, or supply direct measurements of these parameters, such as temperature or SOC [10].

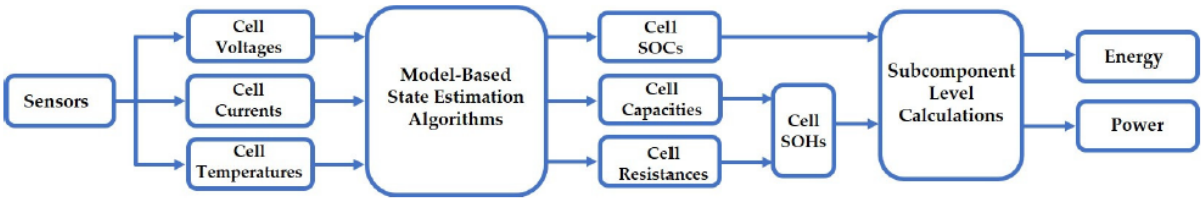

Figure 1: Execution flow diagram of parameter estimation algorithms involved in BMS [1].

Internal temperature measurements can provide information on the distribution of heat generation during different operating conditions, and validate the accuracy of thermal models which are used in research and BMS. Due to the finite thermal conductivity of LIB materials, heat dissipation does not happen immediately, and the internal temperatures will therefore be higher than external temperatures. In addition, the heat generation within a cell is unevenly distributed. Hence, internal temperature measurements can provide a more reliable validation of LIB thermal models [11]. In addition, internal temperature measurements might allow for estimating thermal conductivity changes during cell operation and possibly determine the isotropic nature of the materials' conductivity [7].

Internal temperature measurements of LIB cells require sensors which are electrochemically inert, of small size and corrosion resistant. Optical fiber Bragg grating (FBG) sensors fit these demands. Novais et al. [11] showed negligible degradation of silica based FBGs left in a common electrolyte (LP30) for two weeks. FBGs have been used successfully to monitor internal and external stress and strain of Li-ion cylindrical, prismatic, pouch and coin cells [12][13][14][11][15][16][10]. Novais et al. [11] and Fortier et al. [13] implemented a FBG sensor into a pouch and coin cell and measured single point internal temperature during cycling of the cells. However, as described in section 2.4, FBGs are sensitive to both strain and temperature, and no method to discriminate between the two parameters was used in these papers. Nascimento et al. [15] utilised hybrid sensors consisting of FBGs and Fabry-Perot sensors in series to discriminate between strain and temperature. The sensors was implemented into a prismatic cell, and internal and external temperature and strain was measured during cycling of the cell. However this was an experimental sensor type which is not commercially available. Despite this, optical fibres are fragile and can easily break during implementation into pouch cells [10]. This means that the optical fibres are sensitive to their placement within the pouch cell, and incorrect implementation can result in broken optical fibres that cannot perform as desired. In the studies done on pouch cells, custom cells have been assembled around the optical fiber (OF). A possible reason for this is due to the difficulty of embedding sensors in hermetically sealed cells without damaging the cell packaging and getting a good seal around the OF. However, to use

internal temperature measurements to validate thermal models, it would be beneficial to measure the temperature profile on the cell being modeled and not a custom equivalent cell. In addition, making and assembling custom LIB cells require expensive and specialized equipment. Furthermore, the aging mechanisms of LIBs are complicated mechanisms that are still not fully understood, but known to be dependent on temperature [17]. Thus, it is of interest to investigate the feasibility of embedding FBG sensors in commercial pre-fabricated LIB pouch cells and measure the temperature distribution.

This thesis therefore aims to develop a method for reliably implementing a set of FBGs into a commercial prefabricated LFP cell, discriminating between strain and temperature contributions in order to measure the initial internal temperature during cycling of the cell.

2 Theory

This chapter introduces the basic working principles of LIBs, the most common LIB material chemistries, the basic construction and production of LIBs, an introduction to why temperature is relevant for LIBs and an introduction to OF sensor technology and FBG sensors.

2.1 Battery Chemistry

A LIB cell consists of two electrodes and an electrolyte-soaked separator between them, as shown in Fig. 2. The anode material usually consists of a carbon structure of either soft or hard configuration [18]. The cathode is most commonly made of a lithium transition metal oxide based on cobalt (Co), manganese (Mn), and nickel (Ni), or a combination of these or on a iron (Fe) based polyanion compound. The separator has a porous structure allowing Li-ion diffusion. In addition, the separator is an electric insulator, which allows for an electric potential between the two electrodes.

In secondary LIB, the carbon electrode is referred to as the anode in both the discharge and charge cycle. The transition metal electrode is referred to as the cathode during both discharge and charging cycle. When the cell is discharging, an oxidation reaction occurs on the anode and lithium ions de-intercalate from the anode and migrate through the separator to the cathode, where a reduction reaction occurs and the Li-ions intercalate into the cathode material. Due to the separator, the free electrons from the oxidation reaction are forced to move from the anode to the cathode in an external circuit. When charging, this process is reversed by applying an external electric potential [5].

A LIB operates outside the voltage window where common LIB electrolytes are stable. During the first cycle of a LIB, this results in a side reaction with the carbon anode and decomposition of electrolyte. This creates a passivating layer, which is called the solid electrolyte interface (SEI) layer. A stable SEI layer is important to prevent further degradation of the electrolyte [19].

The cathode consists of a solid host structure which facilitate the intercalation and de-intercalation of Li-ions. The crystal structure of the cathode material is dependent on the chemistry used, and the different crystal structures have an effect on how easily Li-ions can intercalate and de-intercalate, which in turn can effect voltage, capacity, heat generation and the thermal stability. The most common and commercialised cathode chemistries are $\mathrm{LiCoO_2}$ (LCO) and $\mathrm{LiNi_{0,33}Mn_{0,33}Co_{0,33}O_2}$ (NMC) with their layered structure, $\mathrm{LiMn_2O_4}$ (LMO) with its spinel structure and $\mathrm{LiFePO_4}$ (LFP) with its olivine structure [20]. An overview of cathode chemistries are given in Table 1.

LCO is used in the majority of commercial LIBs. It is a high-performance cathode ma-

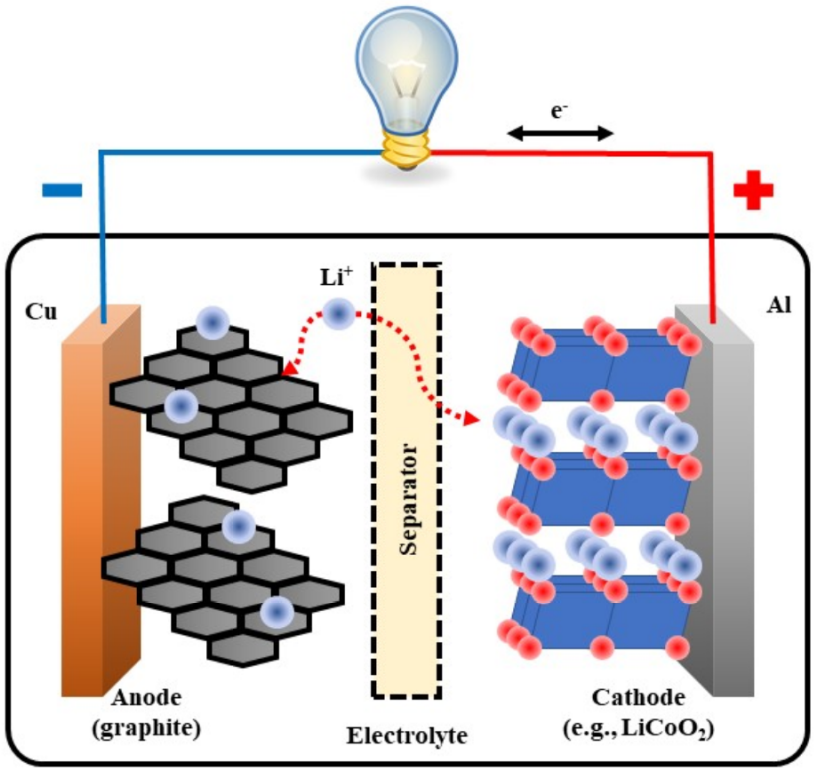

Figure 2: Working principle of Li-ion battery.

terial with high specific and volumetric capacity, low self-discharge, high voltage and good cycling performance [20]. However, LCO is expensive due to the amount of Co required, and it has the lowest thermal stability of the cathode chemistries mentioned here. Thermal stability refers to the temperature needed to reach the onset of thermal runaway. In addition, LCO has fast capacity fade at high C-rates and deep cycling. To improve on this, LCO has been doped with Ni and Mn to produce NMC. This reduces cost, improves on thermal stability and cycle stability at elevated temperatures [20]. The LMO batteries have lower production cost and environmental footprint due to the abundance of Mn compared to Co. However, LMO can suffer from low long-term cyclability due to dissolution of Mn into the electrolyte. LFP has great thermal stability and high-power capabilities. However, LFP has a low average potential, electrical conductivity and ionic conductivity [20].

The anode is commonly made of carbon. However, other anode materials exist, like lithium titanate and silicon-carbon, but are often restricted to special use due to unwanted properties, e.g. the volume expansion of silicon during lithiation of up to several hundred percent [20]. Table. 2 lists the most common anode materials together with their respective advantages.

Carbon is of great abundance and have high electric conductivity, high Li diffusivity and relatively low volume change during lithiation and de-lithiation, which makes it ideal as an anode material. Two distinct carbon anode types exist, graphitic carbon or hard

Table 1: Cathode chemistries overview [2].

LIB Chemistry	Elements	Year	Advantages	Applications
Lithium Nickel Manganese Cobalt Oxide (NMC, $LiNi_xMn_yCo_zO_2$)	Li, Ni, Mn, Co	2008	Good specific energy and specific power density	Battery EVs, power tools, grid energy storage
Lithium Nickel Cobalt Aluminium Oxide (NCA, $LiNiCoAlO_2$)	Li, Ni, Co, Al	1999	High specific energy, good life span	Battery EVs
Lithium Manganese Oxide (LMO, $LiMn_2O_4$)	Li, Mn	1996		Hybrid EV, mobile phone, laptop
Lithium Iron Phosphate (LFP, $LiFePO_4$)	Li, Fe, P	1996	Moderate density (2Ah outputs 70A) High safety Operating temperature >60°C	Personal Transport, power tools, aviation products, automotive hybrid systems, PHEV conversions
Lithium Cobalt Oxide ($LiCoO_2$)	Li, Co	1991	High specific energy	Broad use

carbon. Graphitic carbon have large graphite grains and can achieve close to theoretical charge capacity. However, during lithiation, graphitic carbon can undergo large strain, which damages the SEI layer and reduces cycle life. Hard carbon consists of small disordered graphitic grains, lowering expansion and stress during lithiation. However, a disordered structure of graphene increases the overall surface area resulting in higher loss of lithium during formation of SEI layer, and consequently reduces the cells capacity [20].

Table 2: Anode chemistries overview [2]

Anode	Elements	Year	Advantages	Applications
Graphite	C	1991	Low cost with good energy density.	Main electrode material used in LIB
Hard Carbon	C	2003	Greater storage capacity	Home electronics
Tin-Cobalt Alloy	Co, Sn	2005	Larger capacity than a cell with graphite (3.5 Ah 18650-type battery)	
Lithium Titanate ("LTO", $Li_4Ti_5O_{12}$)	Li, Ti	2008	Good output, charging time, durability (safety, operating temperature 50–70°C, up to 9,000 hours)	Recent commercialised; opportunity charging applications (buses)
Silicon-Carbon	Si, C	2013	Good volumetric energy: 580 Wh/l and can achieve 1.2 Ah/g over 800 cycles	Semi-commercial

The electrolyte works as an ion conductor, and facilitates the movement of Li-ions between the electrodes. It seeps into the porous structure of the electrodes, to facilitate the transfer of ions between the solid electrode and liquid electrolyte. The most com-

mon LIB electrolyte is a non-aqueous solution of lithium salt ($LiPF_6$), dissolved in a solvent which is a mixture of cyclic and linear carbonates [18].

2.2 Physical construction

Secondary LIBs are assembled in four different ways, cylindrical cells, pouch cells, prismatic cells and coin cells. Cylindrical cells consist of a long rectangular single layer cell, which is rolled up and encapsulated in an cylindrical aluminum casing. Prismatic and pouch cells are several stacked layers of electrodes and separators, as showed in Fig. 3. The prismatic stack is encapsulated in a hard-case of aluminium, while the pouch cell is sealed in an aluminium pouch. The coin cell is a small capacity cell with few layers of electrodes stacked and encapsulated in a hard aluminium coin shaped enclosure.

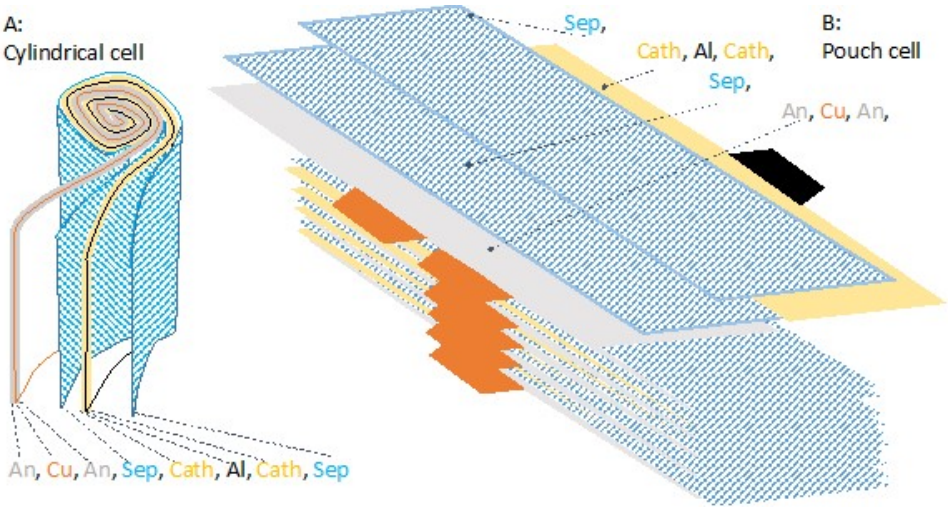

Figure 3: Packaging of Lithium-ion Batteries. Layer stacks of battery components packaged in either a cylindrical cell (A), or a pouch/prismatic cell (B) configuration [2].

The main steps of battery production consists of mixing the raw material, coating it on the current collectors, drying, calendaring, cutting and stacking, packing and activation and storage. In addition to the active material of the electrodes, the mixing process includes carbon black to increase the electric conductivity of the electrodes and binder so the material can adhere to the current collectors and hold the electrode structure together. The energy intensity of the mixing process influences the agglomerate size of carbon black and the overall porosity of the electrode material. This influences the electrodes ionic diffusion ability and electric conductivity. Higher intensity mixing increase electric conductivity and reduces ionic diffusion. Solvent is added into the dry mix to activate the binder and to achieve required viscosity for the coating process. The mixed dry and wet components, called slurry, is then coated onto long roles of the current collector material which is a thin film (5-25 μm) of aluminium for the cathode, and a copper film for the anode. The coating thickness is 40-80μm for the cathode and

50-100 μm for the anode. The electrode thickness is dependent on the configuration produced, thicker electrodes for higher energy density, and thinner for higher power capabilities. Drying of the electrode is done to remove the solvent and complete the adhesion between the slurry and current collector. To obtain the wanted porosity of the electrodes and further secure adequate adhesion between current collector and electrode material, the electrodes are calendared. To prepare the electrodes for assembly, the rolls of anode and cathode are cut into either smaller rolls or patches to make cylindrical or pouch cells. The next step in pouch cell production is stacking the anode, cathode and separator. The stacking can be done by single layers or by winding the separator in a z-pattern between the electrodes. In the case of pouch cells, the terminal tabs are welded onto the current collector tabs, and the cell is inserted into an aluminium pouch. Electrolyte is added to the pouch and the cell is sealed. Before the cell can be assembled into a pack, formation and aging is necessary. The formation process is the first cycling of the cell which forms the SEI layer. The aging process is a quality control where the cells are stored under high temperature followed by normal temperature for up to 3 weeks. The state of charge (SOC) and open circuit voltage (OCV) are monitored to insure the cell is fully functional [21].

2.3 Temperature concerns within a battery pack

Understanding heat generation in LIBs is important since performance and aging of LIBs is strongly linked to temperature [17, 22]. Heat generation in a battery cell is complicated, and many physical phenomena contribute to the heat generation [17]. However, a simplified form, which is widely used in literature and accounts for the heat generation of a complete cell, consists of three heat sources. First is the reversible heat due to entropy change. The entropy change is dependent on SOC and can be both positive and negative, and thus act as both a heat source or heat sink. Second is the internal ohmic resistance of the cell, and the third is heat generation due to overpotential, which is resistance in the chemical reaction. This gives Eq. 1 for heat generation during charging and Eq. 2 for heat generation during discharging [23].

$$q_{ch} = \frac{T\Delta S}{F} j + r_\omega j^2 + \eta j \tag{1}$$

$$q_{disch} = -\frac{T\Delta S}{F} j + r_\omega j^2 + \eta j \tag{2}$$

Here, j is the current density, r_ω is the ohmic resistance,T is the temperature , ΔS is the entropy change over the whole cell, F is the Faraday constant and η is the overpotential.

There are two distinct thermal issues within a LIB cell, which are thermal runaway and accelerated aging. Thermal runaway is the main safety concern of Li-ion batteries. If the cell reaches temperatures above 100 °C, the active material reacts with the organic electrolyte. This is an exothermic reaction, which further increases the temperature if

the heat dissipation is slower than the heat generation [24]. The temperature increase further accelerates the reaction, which releases oxygen, resulting finally in a fire or explosion. Thermal runaway can be activated by mechanical abuse, like puncturing or other stresses which results in a short circuit, or abusive conditions like high voltage or high current. Charging at low temperatures can lead to lithium plating and dendrite growth which can short circuit the cell and develop into a thermal runaway.

Accelerated aging is strongly linked to temperature and results in capacity or power fade. Capacity fade is loss of available energy. Energy or capacity fade can occur when active material inside the battery transforms into inactive phases, called loss of active material, or due to loss of lithium inventory. In both cases available energy is reduced. Power fade is when the cells output voltage is reduced due to increasing internal impedance. This can happen due to several reasons. However, it is clear that elevated operating temperatures accelerates capacity and power fade [17]. It is reported in literature that the main aging mechanism due to elevated temperature is SEI layer growth and consequently loss of lithium inventory [25].

2.4 Fibre optical sensor for temperature measurements

To minimise the invasiveness of a sensor being placed inside a LIB, the sensor needs to be small, chemically inert to avoid reactions with the battery chemistry, non-conductive to avoid short circuits, and corrosion resistant. FBG sensors made of silica fulfills all of these criteria. Corrosion rate of silica in electrolyte is negligible [11], it is non conductive and they have a diameter of 80-125 μm, depending on production method.

OF are electromagnetic waveguides. They are composed of a dielectric material like silica and have a core and cladding. The higher refractive index (RI) of the core enables light to be guided with negligible losses. The basic sensing mechanisms of an OF sensor is modulation of light properties (e.g., phase, intensity or polarisation), as it is transmitted through the OF. Modulation of the light is achieved either intrinsic, where the light properties are altered due to internal changes of the OF parameters caused by external stimuli, or extrinsic, where a change in RI or absorption in the surrounding media causes the light modulation [26]. Temperature sensors are in general intrinsic, due to the inherent cross-sensitivity of temperature to other parameters in extrinsic sensors [27]

In general an OF sensing setup consists of a light source, the sensor, a detector and conversion to electrical signal [3]. Fig. 4 show the general components needed for a OF sensor setup.

The FBG sensor is a suitable sensor for internal measurements of LIBs and has been used successfully in several papers [7, 11, 13, 14, 15, 16]. The FBG sensor consists of periodic RI modulations in the core, along the axis of the OF. The gratings are created by, precisely and for a short time period, exposing the desired grating area with UV

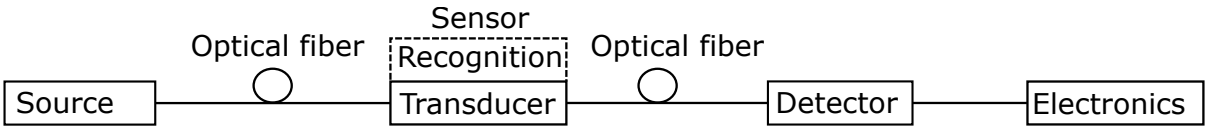

Figure 4: General components needed for a sensor setup[3].

light. The total length of the grating section is shorter than 100 μm. The RI modulations create an interference pattern which reflects a narrow wave length band. The FBGs are suited for low invasive use in LIBs due to the reflection of the signal of interest. This allows for only one entrance point per OF in the LIB, as shown in fig 5.

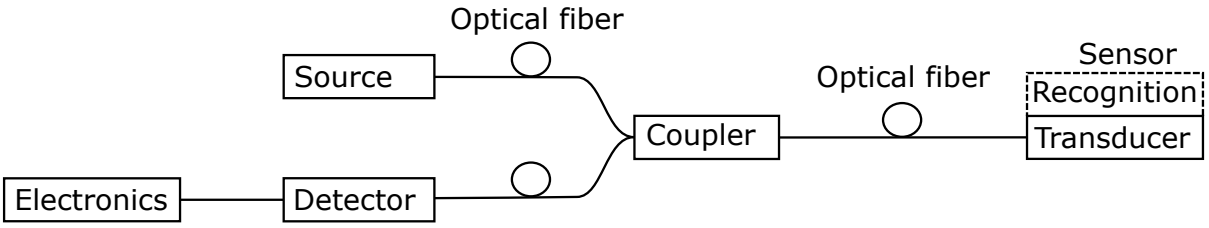

Figure 5: General components needed for a reflection sensor setup[3].

The central wavelength of the reflected wavelength band is the Bragg wavelength (λ_B), which is given by

$$\lambda_B = 2N_{\mathit{eff}}\Lambda, \tag{3}$$

where N_{eff} is the effective RI and Λ is the distance between the the modulations, i.e. the period [7]. Both N_{eff} and Λ are temperature and strain sensitive according to

$$\Delta\lambda_B = 2\left(\Lambda\frac{dN_{\mathit{eff}}}{dT} + \frac{d\Lambda}{dT}+\right)\Delta T + 2\left(\Lambda\frac{dN_{\mathit{eff}}}{d\varepsilon} + \frac{d\Lambda}{d\varepsilon}\right)\Delta\varepsilon, \tag{4}$$

where T is temperature and ε is strain. A change in temperature or strain will therefore both result in a shift of the reflected wavelength (λ_B), as shown in fig 6.

Since the temperature dependence on λ_B is linear and without hysteresis, calibrating is done by taking λ_B measurements at different known temperatures and applying linear regression to the data in order to link the λ_B to temperature. A typical FBG sensor has a sensitivity of 10 pm shift in reflected wavelength per 1°C and 1 pm shift in reflected wavelength per 1$\mu\varepsilon$. To be able to detect such small shift in reflected wavelength, a Gaussian fit is performed on the reflected signal to identify the central wavelength. This allows for a high number of sensors to be placed in series on one OF, creating a sensing array.

As the FBG is sensitive to both strain and temperature, discriminating between the temperature contribution is a challenge. This can be solved by using two sensors in close proximity on the same OF and with high difference in strain and temperature response. By using the matrix equation

$$\begin{pmatrix}\Delta\lambda_1\\ \Delta\lambda_2\end{pmatrix} = \begin{pmatrix}K_{\varepsilon 1} & K_{T1}\\ K_{\varepsilon 2} & K_{T2}\end{pmatrix}\begin{pmatrix}\varepsilon\\ T\end{pmatrix} \tag{5}$$

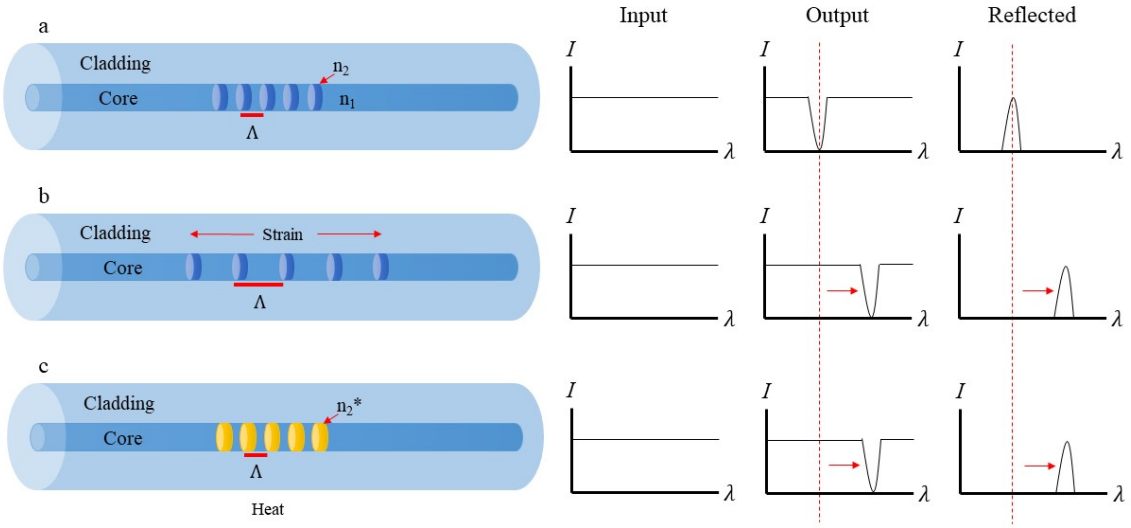

Figure 6: Schematic of FBG measuring modes. A FBG with no strain and ambient heat will have a specific output and reflected profile (a), as strain is applied, due to temperature, pressure or bending, the grating spacing will change (b), and/or the refractive index of the grating (n_2^*) will change (c) causing a shift in the output and reflected signal.

and inverting the equations, one can obtain temperature and strain from the wavelength shifts $\Delta\lambda_1$ and $\Delta\lambda_2$. Another approach is to isolate one sensor from either strain or temperature and use as a reference to subtract from the wavelength shifts on the other sensors on the same array [28].

In large LIB cells one FBG array could be placed in a winding pattern to obtain a temperature distribution. However, in smaller cells the minimal bending radius of the OF would prevent this. Fig 7 shows an experimental setup with three OFs, each with three FBGs, creating a sensor array. Optical-fiber couplers are used to connect the FBGs to the IR source and return the reflected signal to the detector.

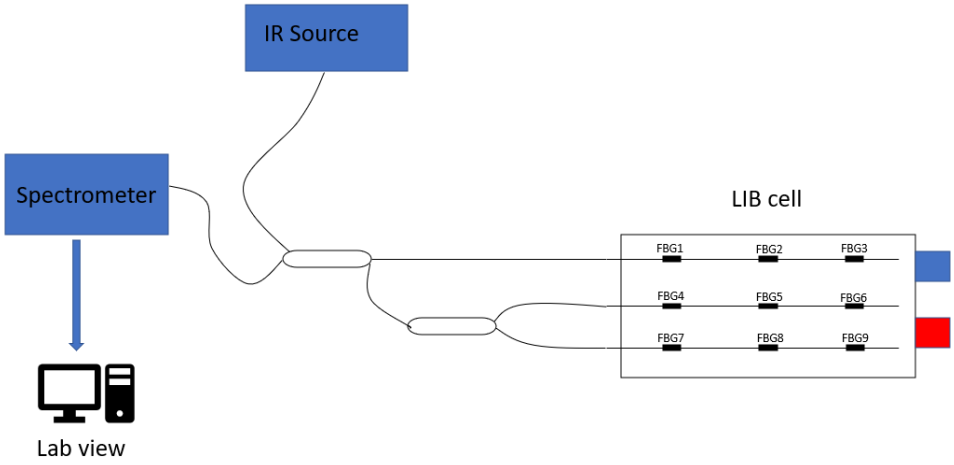

Figure 7: Experimental setup.

3 Experimental

This section describes the materials and methods used to arrive at a final implementation procedure which can be used to install glass capillaries or OF into a LIB. In addition, the setup for the FBG calibration and measurement setup is described.

3.1 Pouch Design

To isolate the FBGs from strain contributions, glass capillaries was used. The capillaries prevent strain from effecting the sensors while conducting heat. The capillary implementation method used was based on suggestions from a project paper [29] written by the author of this thesis. The battery cell used as test object was a 4 Ah LFP pouch cell with external dimensions 9.6*50*127 mm. The original cell pouch and interior of the cell prevents direct implementation trough modification of the original pouch as previously discussed in [29]. A new pouch assembly was used as shown in Fig. 8.

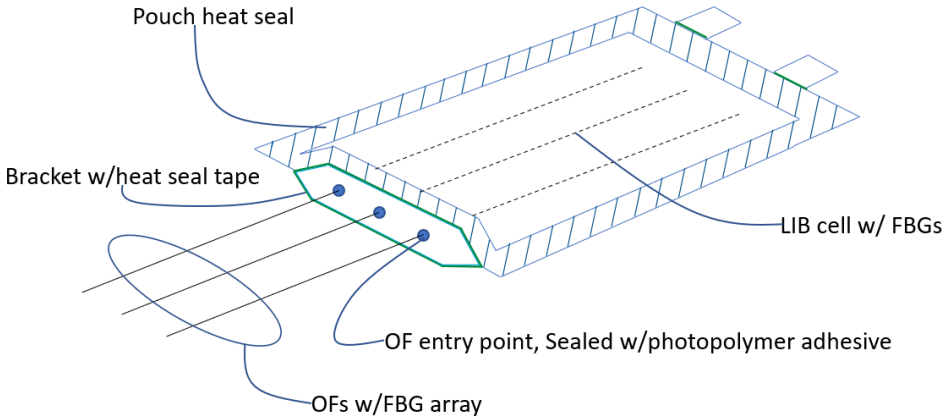

Figure 8: New pouch concept

The bracket is there to ensure accurate positioning of the capillaries and to avoid breaking the capillaries in the pouch seal, as experienced by others [7, 10]. The bracket was 3D-printed with 100% infill in the material polypropylene (Ultimaker PP) to ensure it would not corrode due to contact with the electrolyte. To enclose the bracket in the laminate pouch material (Targray aluminium laminate, PC 8) and seal around the battery tabs, an etehylene-vinyl-acetat (EVA) based hot-melt glue was used (Fastel Film, mod 16071). The dimensional design of the bracket, heat and time settings on the double sided heat sealer (Audion 421 MGMISDS) was found trough an iterative approach. The seal was evaluated by filling the pouch with water and an external pressure was applied to see if water was escaping the pouch. Another quality feature of the seal that was used is the reduction of laminate thickness specified by the supplier to be at around 30%. In addition, the the seal was re-opened and inspected visually so areas

prone to leaking could be detected and improvements made. To secure the capillaries in the bracket and make an airtight seal, photo polymer adhesive (Norland NOA65) was used, and cured with a hand held LED UV light source (Nordland Opticure led 200).

3.2 Implementation procedure

A total of 5 attempts where made to implement capillaries into a LFP cell. In addition, an initial practice run was made using single mode OF instead of capillaries. The implementation procedure described below is the initial method used. In section 4.2, changes that where made due to insufficient performance, such as pouch leaks and breaking of capillaries, is presented and discussed.

The bracket was sanded with 220 grit sandpaper to remove surface channels running normal to the seal direction on the bracket which could facilitate moisture ingress or electrolyte egress. The bracket was then wrapped with Fastel Film and and an extra flank of Fastel Film of minimum 5 mm from the bracket edge was added. Before sealing the bracket and two edges of the pouch, the internal pouch material was cleaned thoroughly with 96% ethanol.

The capillary used (Molex Poly Micro Capillary Tubing, 106815-0024) had a polymide coating. This was removed with a propane torch to reduce the outer diameter of the capillaries from 360 μm to 340 μm. The capillaries was capped at one end with UV glue and a 10 mm long OF as shown in Fig. 9

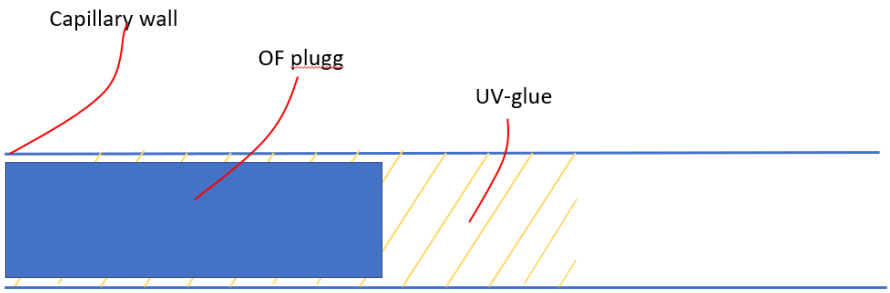

Figure 9: Plugging of one end of the capillaries.

The pouch and capped capillaries were introduced into a glovebox with argon atmosphere. Before implementation the cells were discharged to the cell suppliers recommendation of 2.5 V. The original pouch of the LPF cell was removed and the capillaries were placed in the middle layer of the cell, between the separator and anode, as shown in Fig. 10. The pouch was sealed using a vacuum chamber sealer (AUDIONVAC VMS 53). Fastel film was also used as around the tabs.

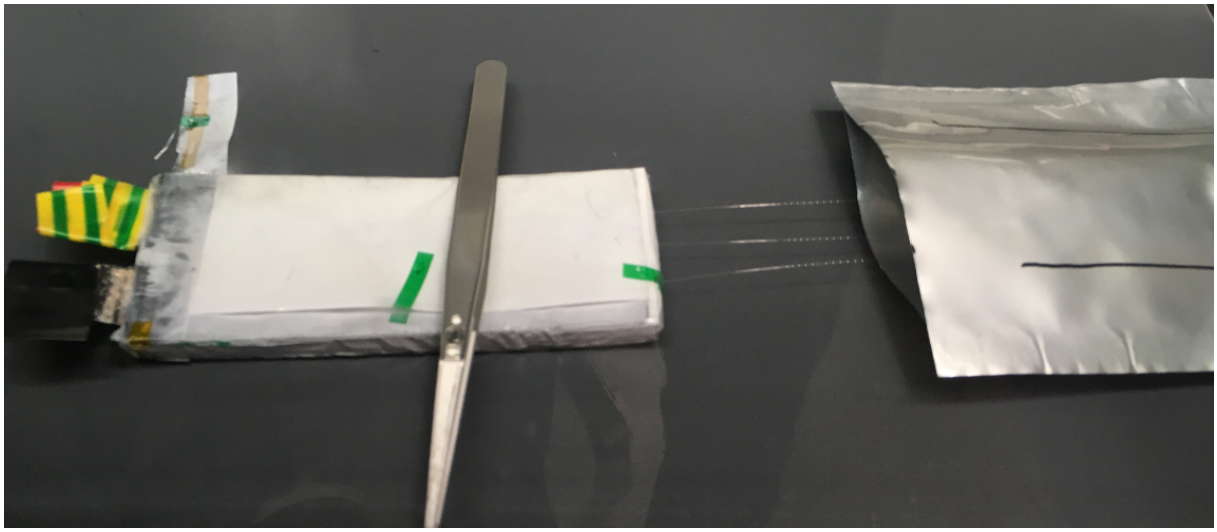

Figure 10: Capillaries placed in the middle of the cell. The cell was pushed into the pouch while the capillaries slid trough the bracket at the other end of the pouch.

3.3 Leak detection

In order to cycle the cells and assess the effect of the capillary implementation, the cell needs to be hermetically sealed to prevent moisture ingress or electrolyte egress. Moisture ingress can lead to formation of hydrogen fluoride (HF) that can attack the cathode material and result in cell degradation. Electrolyte egress reduces the amount of electrolyte in the cell and causes deterioration of cell performance [10]. Moisture ingress or electrolyte egress can give false indications on the invasiveness of the capillaries. After implementation the cells where monitored while still in the glove box. The cell was visually inspected to see if the pouch relaxed due to pressure equalisation and the OCV was measured. In addition, OF was inserted into the capillaries to see if they where mechanically intact. The cells where then moved to a fume hood where the OCV was monitored. The OCV of the cells with capillaries were compared to an unaltered cell which had been discharged in the same manner as the cell with capillaries.

3.4 Capillaries invasiveness

In an attempt to identify the the impact of the capillaries on the cells, the cell was characterized with an Arbin battery tester before and after implementation. The capacity of the cell was measured at 1 C and internal resistance (Ri) was measured at five SOC points trough hybrid pulse power characterisation (HPPC).

Measuring Ri by the HPPC method is based on a second order equivalent circuit model [30]. The schematic of the model is shown in Fig. 11.

R0 represents the ohmic losses of the cell. R1 and C1 represents the reaction re-

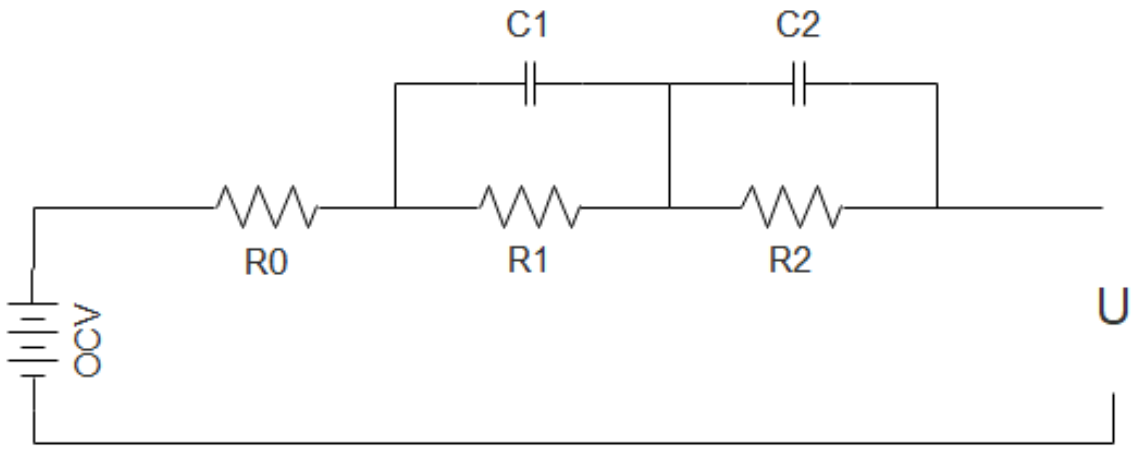

Figure 11: Circuit-based model of battery.

sistance or the Tafel overpotensial and R2 and C2 represents the concentration overpotensial and Rt is the total resistance. A series of 10 second long current pulses is drawn from the battery at different SOC levels. Fig. 12 shows an example of one pulse.

The values Rt, R0, R1, and R2 are calculated by Eq. 6, 7, 8 and 9:

$$Rt = (U0 - U3)/\Delta I \tag{6}$$

$$R0 = (U0 - U1)/\Delta I \tag{7}$$

$$R1 = (U1 - U2)/\Delta I \tag{8}$$

$$R2 = (U2 - U3)/\Delta I, \tag{9}$$

where U0, U1, U2, U3 and ΔI corresponds to the voltage drop and current drop shown in Fig. 12

3.5 FBG calibration

The setup used to calibrate the FBGs is illustrated in Fig. 13.

The FBGs used were placed inside capillaries during calibration so the calibration setup would equal the measurement setup and to ensure no strain was contributing

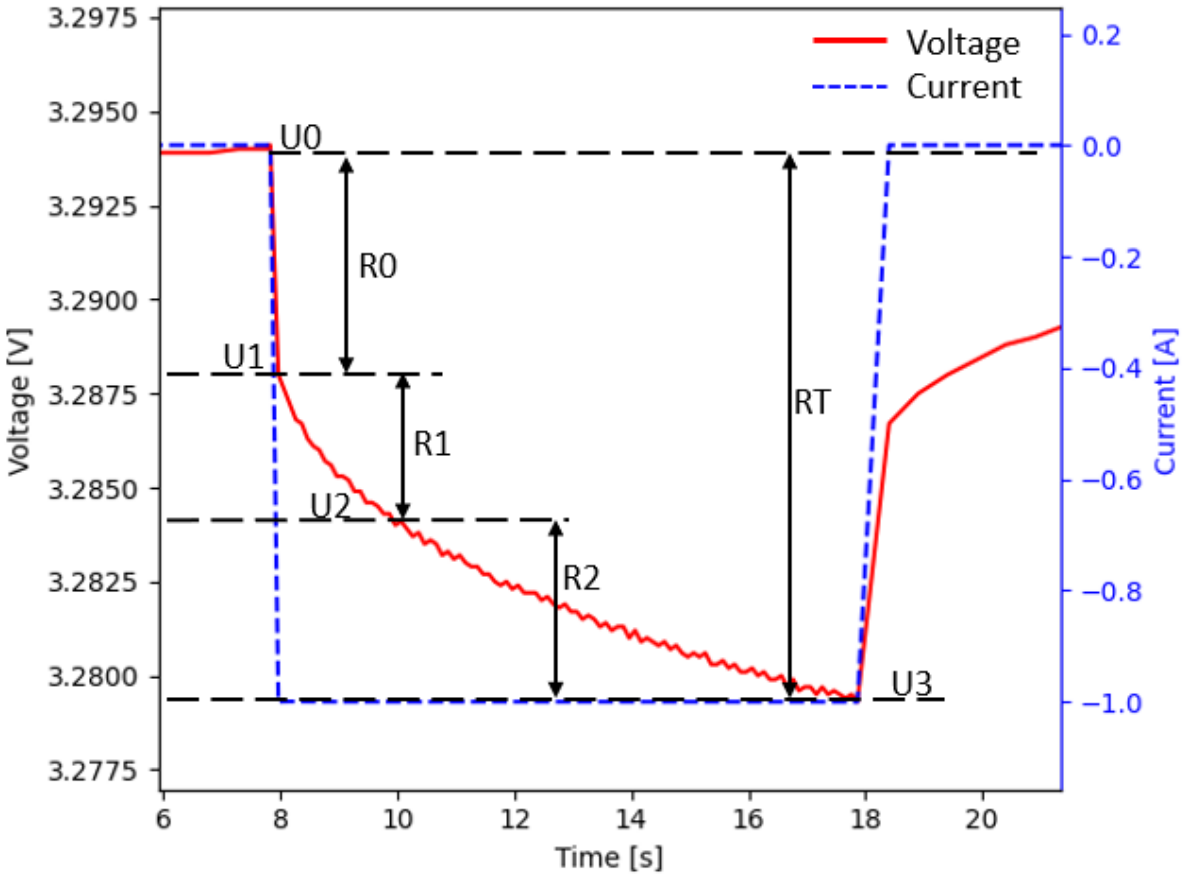

Figure 12: Voltage and current of HPPC pulse.

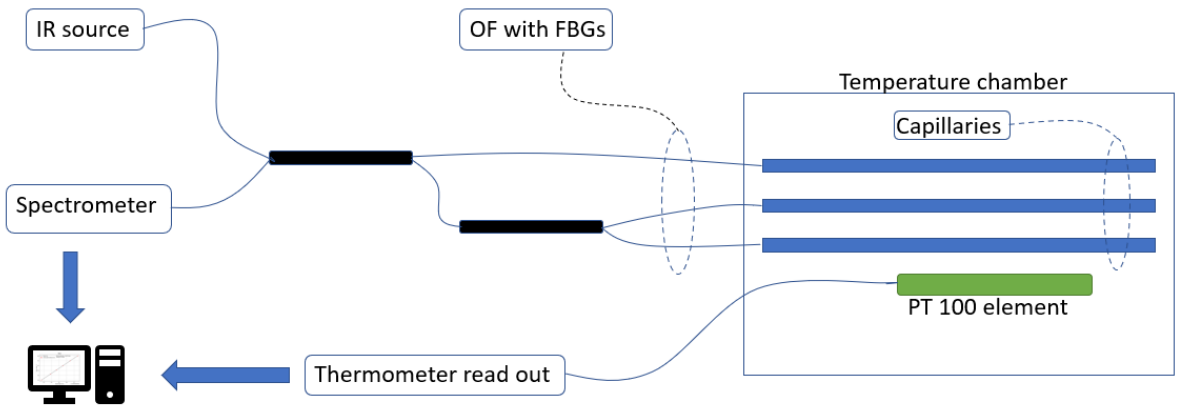

Figure 13: FBG calibration setup.

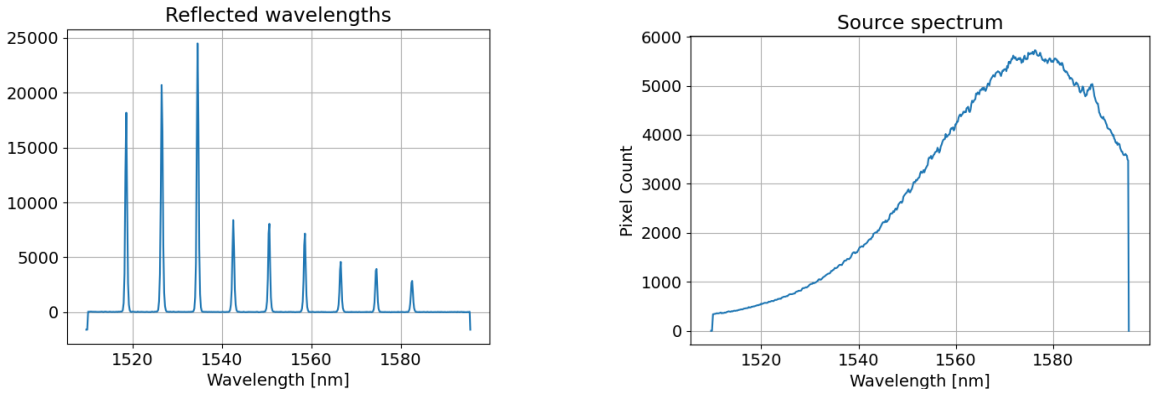

Figure 14: Reflected wavelength spectrum and source spectrum.

to the wavelength shift of the Bragg wavelength. The capillaries with FBGs inside was placed in a temperature chamber (Memmert, Climate Chamber ICHeco) together with a reference temperature sensor in close proximity to the FBGs. The dampening of the signal, due to 50:50 splitting in the optical couplers, reduced the amplitude on two of the three FBG arrays. So a spectrum sample of the IR source was made to best match the strongest part of the source spectrum to the FBG arrays with the highest dampening. The light source spectrum and reflected wavelengths are shown in Fig. 14.

As seen in Fig. 14, the signal loss in the optical couplers was greater then the amplitude variation in the source spectrum. This resulted in a lower accuracy for two of the three FBG arrays, as can be seen in the calibration summary in Table 3.

Bragg wavelength measurements where made at at 6 different reference temperatures in the interval 10-60 ℃. At each reference temperature at total of 120 spectrum samples and 60 temperature samples where made. A Gaussian fit was made to each of the reflected spectrum peaks and the central wavelengths were averaged over the 120 samples. One of the fitted curves is shown in Fig. 15.

A linear fit was performed for each FBG and Fig. 16 shows a calibration for one of the FBGs. In table 3 relevant calibration results is listed.

The calibration showed an excellent linear wavelength shift in response to temperature. For the 9 FBGs, the sensitivity was recorded to be between 0.100 and 0.106 ℃/pm and with a precision between $\pm$ 0.0007 and 0.0014 ℃/pm. However, the maximum deviation from the regression lines varied between the FBGs, with the lowest maximum at 0.29 ℃ and highest maximum at 0.75 ℃. Fig. 17 shows the deviation for FBG 8. The average deviations for the whole temperature range, RMSE, was between $\pm$ 0.21 ℃ and 0.45 ℃. The accuracy obtained by the calibration of the FBGs corresponds well with typical wavelength accuracy of the spectrometer at $\pm$ 5 pm. The typical accuracy of the spectrometer results in an temperature accuracy of approximately $\pm$ 0.5 ℃.

Table 4 shows specifications on the FBGs and equipment used for calibration and

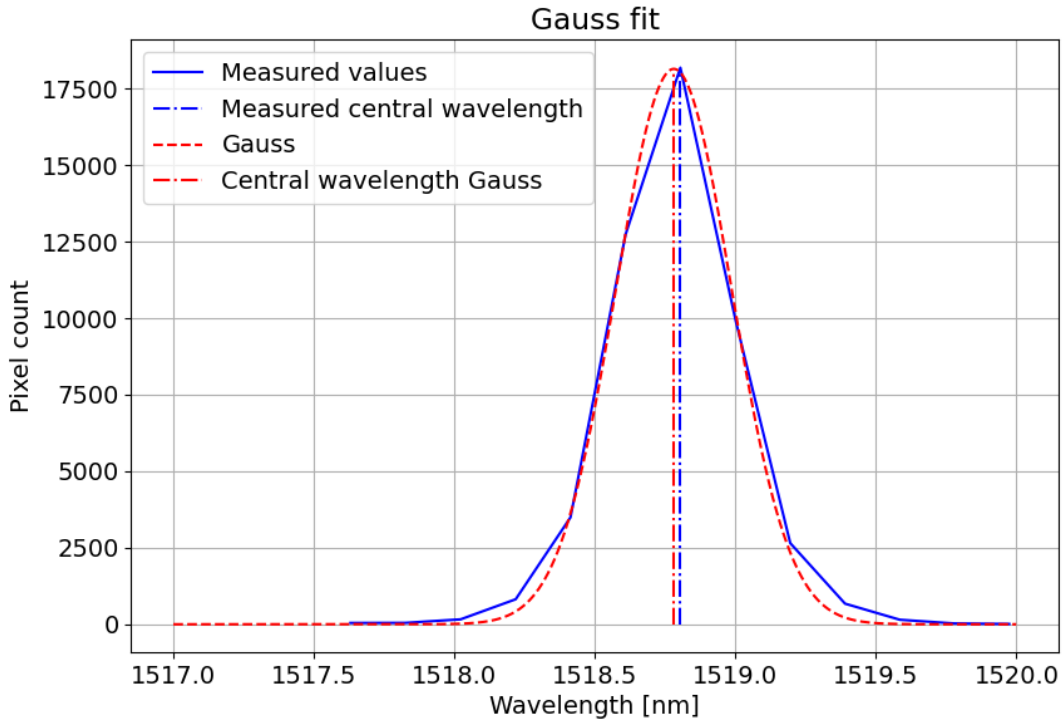

Figure 15: Gaussian fit to the spectrometer data to obtain the center wavelength.

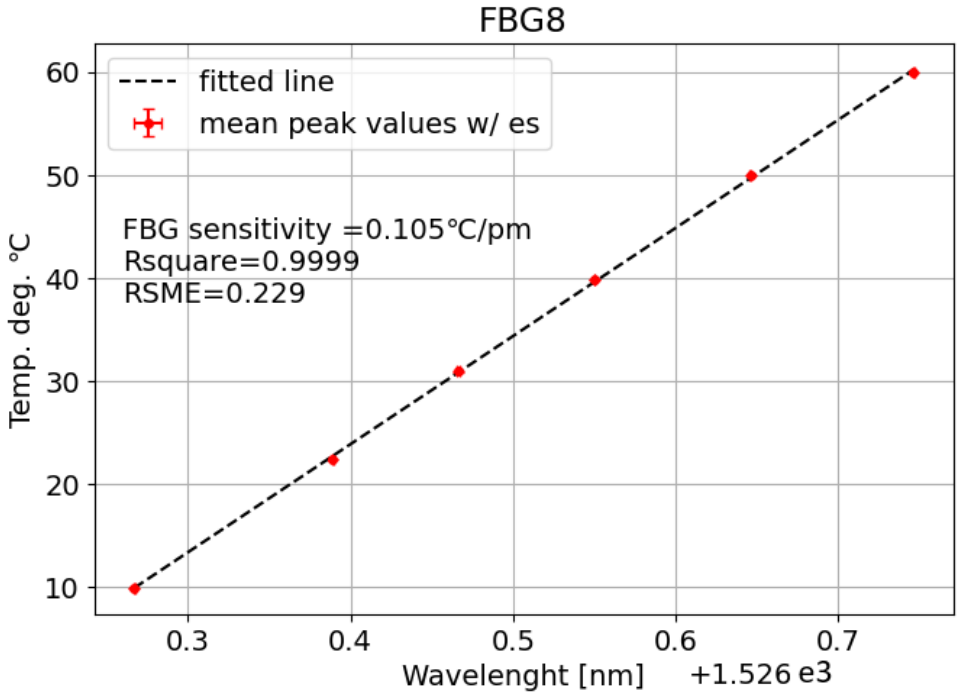

Figure 16: Typical fitted line for one of the nine FBGs.

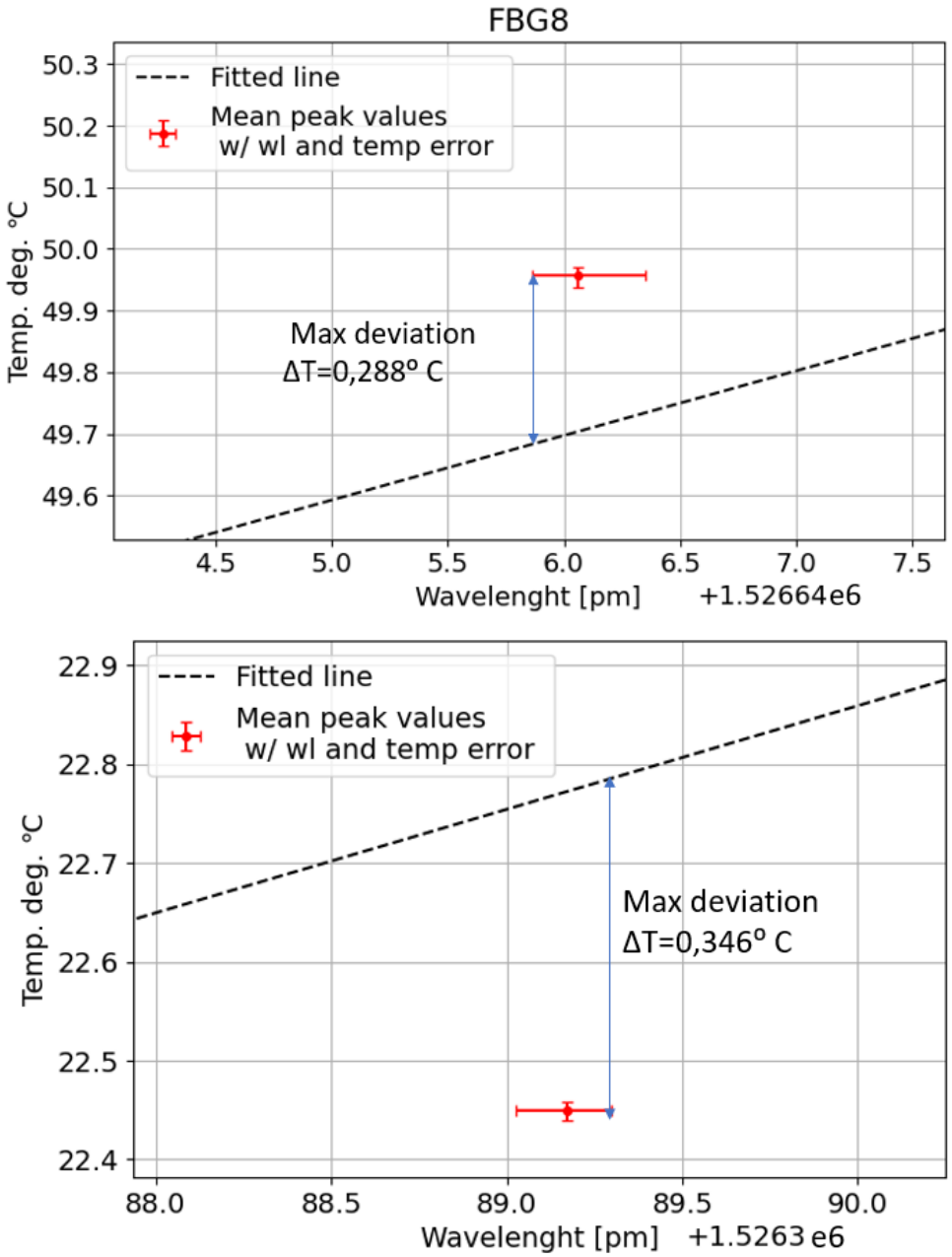

Figure 17: Example of upper and lower maximum deviation from one FBG.

Table 3: Calibration results.

FBG central wl [nm]	Sensitivity [C/pm]	r value	Std err [C/pm]	RMSE[C]	MAX dev [C]
FBG array 1					
1518	0.106	0.9999	0.673e-3	0.211	0.350
1526	0.105	0.9999	0.719e-3	0.229	0.346
1534	0.105	0.9999	0.832e-3	0.264	0.487
FBG array 2					
1542	0.104	0.9996	1.411e-3	0.450	0.751
1550	0.106	0.9997	1.216e-3	0.384	0.674
1558	0.103	0.9998	1.153e-3	0.372	0.705
FBG array 3					
1566	0.101	0.9999	0.822e-3	0.271	0.482
1574	0.101	0.9998	1.077e-3	0.356	0.496
1582	0.100	0.9998	0.961e-3	0.319	0.599

Table 4: FBG equipment specifications.

Equipment	Suplier	Model	Spec
FBG Array	Fisense		Number of FBG: 3 OF diameter: 0,125mm Reflectivity: >50%
IR Source	Thorlabs	SM benchtop SLD source	wavelength: 1550 nm bandwitdth: 50nm
Spectrometer	Ibsen photonics	I-mon 512 USB	Wavelength range: 1510-1595 nm Wavelength accuracy: 5 pm Measurement frequency: 3000Hz
Couplers	Thorlabs	50:50 Wideband Coupler 1x2 and 2x2	Center wavelength: 1550nm Signal Output: 45,0%-55,0% Tap Output: 45,0%-55,0%
Reference Thermometer	Fluke	1502 A	Range: -200 to 962 C accuracy: +/- 0,0006 C at 0 C +/-0,0009 C at 100 C

temperature measurements.

3.6 Internal temperature measurements

The measurement setup was similar to the calibration setup, with the exception of the capillaries were inside the LFP cell and one capillary fixed on the surface of the cell, as shown in Fig. 18. An FBG array was inserted into one of the internal capillaries of the LFP cell. In addition, a capillary was fixed to the outside of the cell directly above the internal capillary and an FBG array inserted. To complement the external FBG array, a PT100 sensor was fixed to the cell surface while another PT100 sensor measured the ambient temperature. The cell was cycled at different C-rates with 30 min rest between charge and discharge. The charging cycle was done at 0.5 C CC and 3.55 V CV. The discharge rates where 0.5, 1, 1.5 and 2 C with cutoff voltage at 2.5 volts.

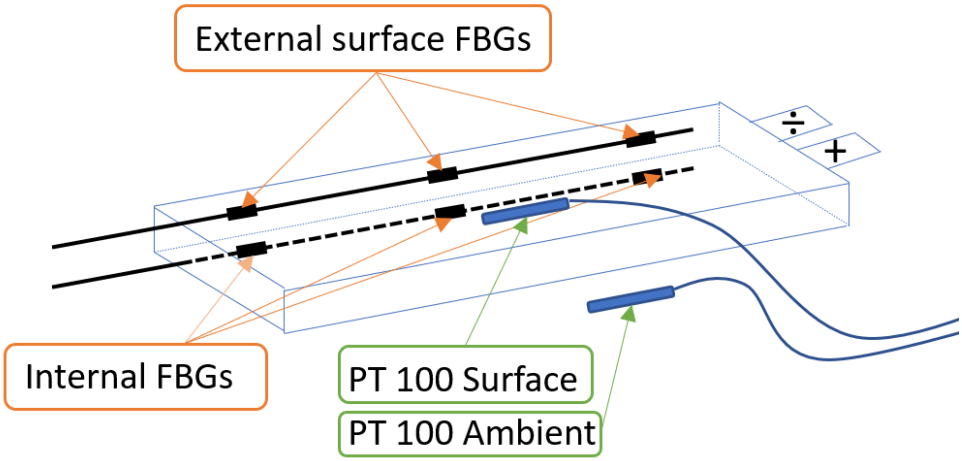

Figure 18: Illustration of sensor locations during temperature measurements.

The signal received from the spectrometer was normalised to the PT100 element measuring ambient temperature. In addition the signal was smoothed using a Savitzky–Golay filter. This particular smoothing method was chosen to increase the precision of the signal without distorting the signal tendencies [31]. Fig. 19 show the smoothing and normalisation process. The first graph is with no smoothing or normalisation. The second graph is with the Savitzky–Golay filter applied and the last graph the signal is normalized by taking the average deviation from the PT100 element measuring ambient temperature and subtracting that value from the signal. The deviation was measured over a period of two hours and the cell had rested in ambient temperature for more then 24 hours before the measurement was made.

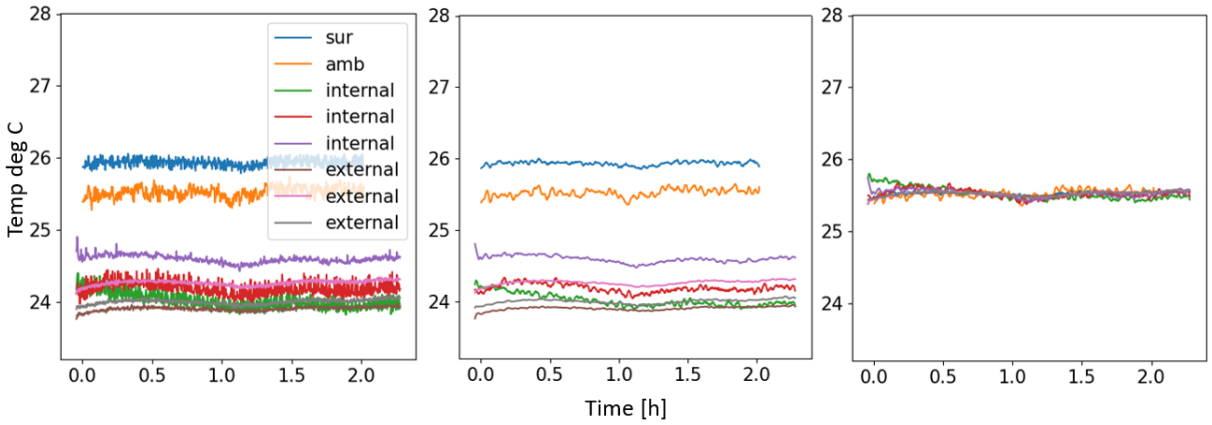

Figure 19: Smoothing and normalization of temperature signal.

4 Result and Discussion

In this chapter the results from the implementation process, the effects on the cell and temperature measurements are presented and discussed.

4.1 Bracket design

As mentioned in section 3.1, a polypropylene bracket was used to protect the capillaries from the sealing bar pressure and align the capillaries during sealing. Table 5 highlights the iterative approach used to arrive at the current design.

Table 5: Pouch development process.

TEST	Result	Error mode	Error cause	Correction
1	No Seal	Sealer did not close	Bracket to thick	Reduce bracket thickness to 2mm
2	Poor seal	Not visible compression of pouch laminate on bracket flanks	Too low flexibility in heat sealer band to apply adequate pressure on bracket flanks	Change geometry, one side flat and flank length increased so the flexibility of the sealer bar gets full contact with bracket
3	Poor seal at corner	Low adhesion of pouch laminate	To little laminate material available for sealing due to interference from bracket	Reduce total width of bracket while keeping flank width, increasing laminate with to 95 mm
4	Poor seal, water leak	Seal failure at transition from heat glue adhesion to laminate adhesion	Too small amount of heat glue	Extend heat glue overlap at bracket end
5	Poor seal, water leak	Failure of adhesion between bracket and heat seal glue	Too low heat during sealing	Increase heat in sealer and compression time

Some of the results related to development of the bracket is equipment related. So other approaches may have to be used with different sealers and other cell dimensions. However, some general observations where made that ensures an adequate seal. Firstly, one should expect a compression of the laminate on the entire length of the seal, as specified by the laminate supplier. Secondly, the amount of heat seal tape used should be enough for the melted tape to reach the adhesion zone of the laminate at full width of the laminate seal. Unless this happens a wedge shaped area of no adhesion is formed at the intersection between the laminate seal and heat-seal tape seal. This area is a likely point of failure and was the origin of leak during test 4. Finally, the heat used during sealing should be high enough so that when ripping the seal apart the adhesion strength between the tape, polypropylene and laminate should be higher than the tensile strength of the tape material. This results in the destruction of the tape and not the bond when separating the materials.

4.2 Implementation procedure

A total of 5 attempts where made to implement capillaries into a cell. Between each attempt, the result was evaluated and improvements made. The initial control of the results was done trough visual inspection and OCV surveillance. The measured values is shown in Fig. 20.The Three first cells showed reduction of OCV after being removed from the argon atmosphere and introduced to atmospheric conditions. This indicates

ingress of moisture and HF production. These cells were deemed unfit for further testing. Cells 4 and 5 showed stable OCV after introduction to atmospheric conditions and were initially cycled at low C rates to further evaluate the cells.

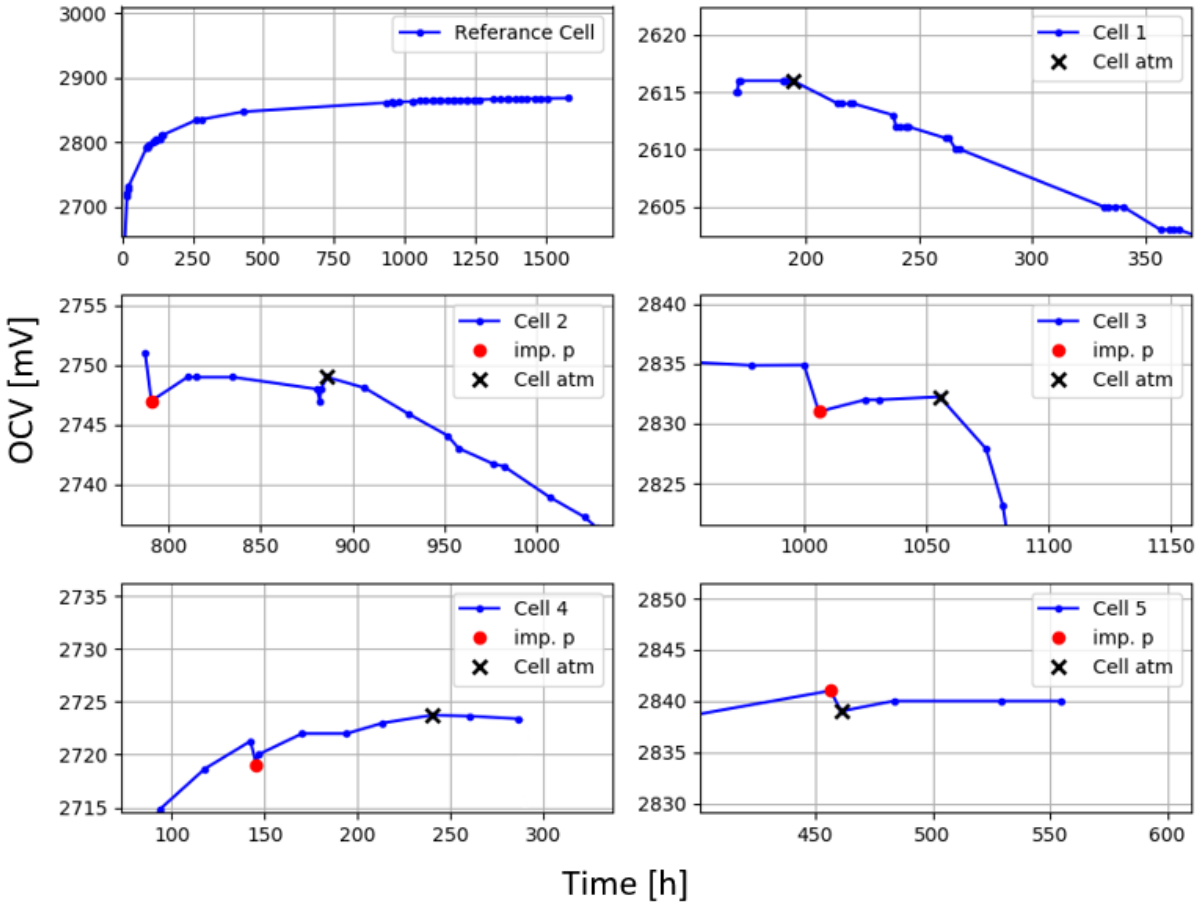

Figure 20: OCV vs time of cells.

Between each cell, improvements where made. When the first cell indicated leaks the cell was re-opened in an attempt to identify the cause of the leak. It was discovered that the OF was broken in addition to the leak. This indicated that the cell was not perfectly aligned with the entry point of the OF. To give the capillaries the opportunity to slightly move or bend during the vacuum sealing, the distance from the bracket to the cell was increased in the second attempt. In addition to moving the cell, it was observed a weak bond between the tabs and heat sealing glue on the side which is not in direct contact with the heating elements in the sealer. Since the dwell time used on the sealer was on the max setting, cell 2 was sealed twice, one on each side of the tabs.

Cell 2 also experienced a drop in OCV after introduction to atmospheric conditions. 1 out of three capillaries broke during sealing and was plugged while inside the glove-box. During the sealing process it was observed that the pouch laminate slightly twist due to the pressure gradient which moves the bracket relative to the cell and could

cause the capillaries to break. The adhesion between the tabs and the heat seal tape on cell 2 was observed to be low, despite the double sealing. For cell 3 the vacuum pressure was reduced to -0.5 bar and the tabs were cleaned with ethanol outside the glove-box prior to sealing.

Cell 3 experienced the most aggressive leak of all the cells. The leak was visually detected to be between the tabs. The pressure applied by the sealing bars in the vacuum sealer is directly linked to the amount of vacuum in the chamber. Hence, the vacuum reduction resulted in a reduced sealing pressure which is critical for a high quality seal [21, 32]. However, all the capillaries survived due to the reduction of vacuum.

For cell 4, the vacuum pressure was increased to -0.6 bars and the amount of hot-melt glue was increased to fill the voids present due to low sealing-bar pressure. In addition, cleanliness of the seal area is a quality factor [21] so the tabs and pouch were cleaned a second time inside the glove-box with DMC. As EVA-based adhesive have a relative low adhesion strength to copper and aluminum [33], the tabs where sanded with 220 grit sandpaper in an attempt to increase the adhesion.

Cell 4 showed promising OCV values at the point of exposure to atmospheric conditions and all the capillaries had survived. The cell was initially cycled at low C-rates, 1/10 C, to see if the cell remained sealed. Before one cycle could be completed the seal failed completely. As the whole length of the seal failed, it indicates that the FastFilm is not suitable for use in LIBs as heat-seal tape, and a tape specifically made for LIBs should have been used. However, for cell 5 it was attempted to further increase the sealing bar pressure by increasing the vacuum to -0.7 bars.

Cell 5 showed excellent OCV stability after exposure to atmospheric conditions. However, as it was required to set the vacuum pressure to -0.7 bars to obtain enough sealing-bar pressure, two out of three capillaries broke. The defect capillaries where plugged to prevent moisture ingress or electrolyte egress. Cell 5 also survived the initial cycling and was further cycled with one internal FBG array. However, after HPPC and temperature measurements the OCV of cell 5 showed similar drop as that of cell 2 and 3. This indicates moisture ingress sometime during the HPPC or temperature measurements.

The issues with leaking cell can be addressed by changing out the heat-seal tape. In addition, by leaving a small part of the long edge of the pouch open while sealing the the tab edge, full sealing bar pressure can be used without damaging the capillaries. Then lower pressure can be used to seal the remaining opening.

4.3 Procedure effect on cell Performance

The capacity and internal resistance (Ri) was measured before and after implementation of the capillaries. As the procedure resulted in evaporation of electrolyte solvents during the pouch swap, and solvent refilling was done with only DMC, it was expected that the characteristics of the cell would change. The results showed a capacity reduction of 10%, as shown in Fig. 21.

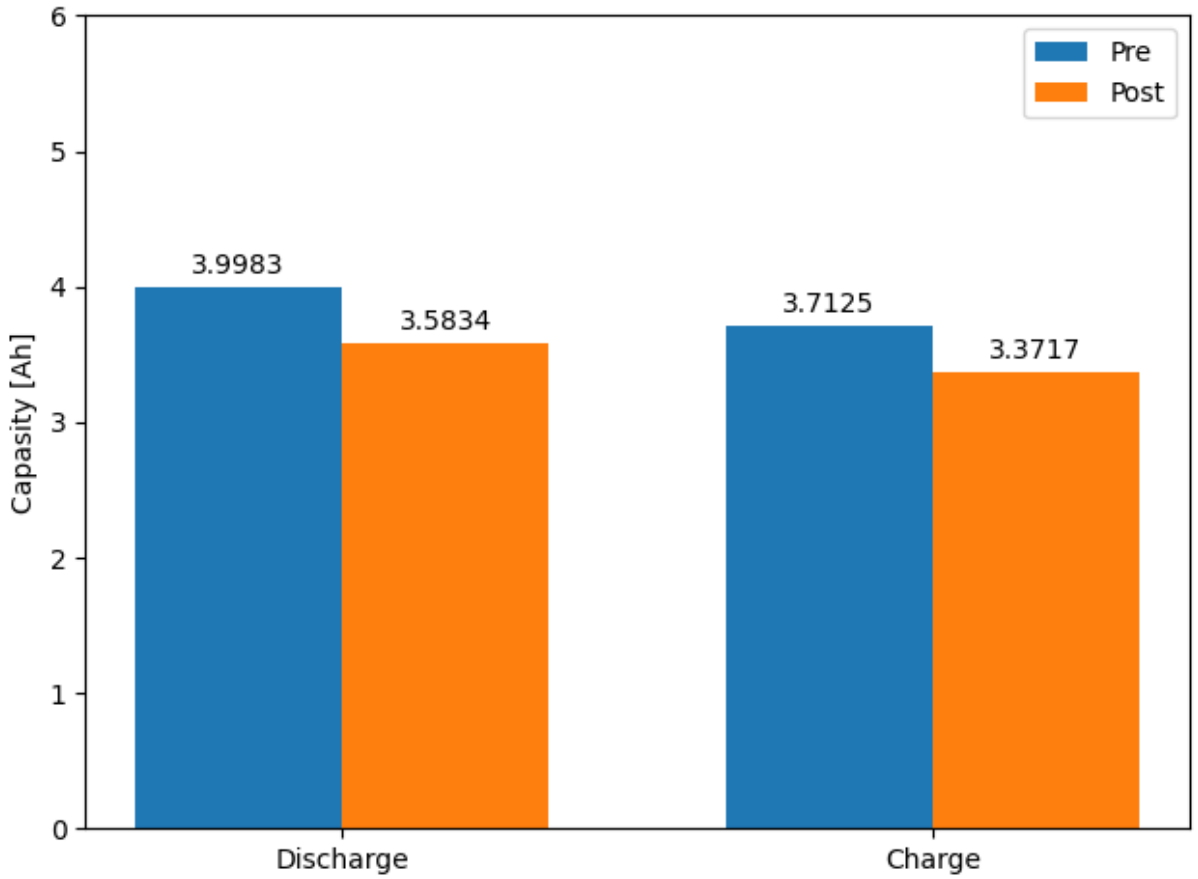

Figure 21: Charge/discharge capacity prior to the implementation of glass capillaries and after implementation, showing a 10% reduction in capacity.

Björklund et al. [34] investigated electrolyte performance with different amounts of DMC. The capacity drop from an LP40 electrolyte to an electrolyte with 100% DMC as solvent was approximately 10%, which corresponds well with the observed capacity reduction. However, this does not prove whether or not the presence of capillaries influence the cell capacity. If the thickness of the capillaries is large enough to effectively split the cell in half, the capacity would only be reduced by 1/38. So it is safe to assume that the capacity drop is mainly due to the change in the electrolyte composition.

Trough a HPPC, the internal resistance was measured before and after implementation of capillaries. Results are shown in Fig. 22. R0, which is dominated by the omhic

resistance, was reduced over the whole SOC range after implementing the capillaries. However, a more expected result was observed for R1 and R2 which increased over the whole SOC range. This resulted in the Rt to be unchanged in the range 60-100%SOC and increase by 17% and 7% at 20% SOC and 40% SOC respectively. Regarding the changes made to the cell one would expect an increase of all resistance values.

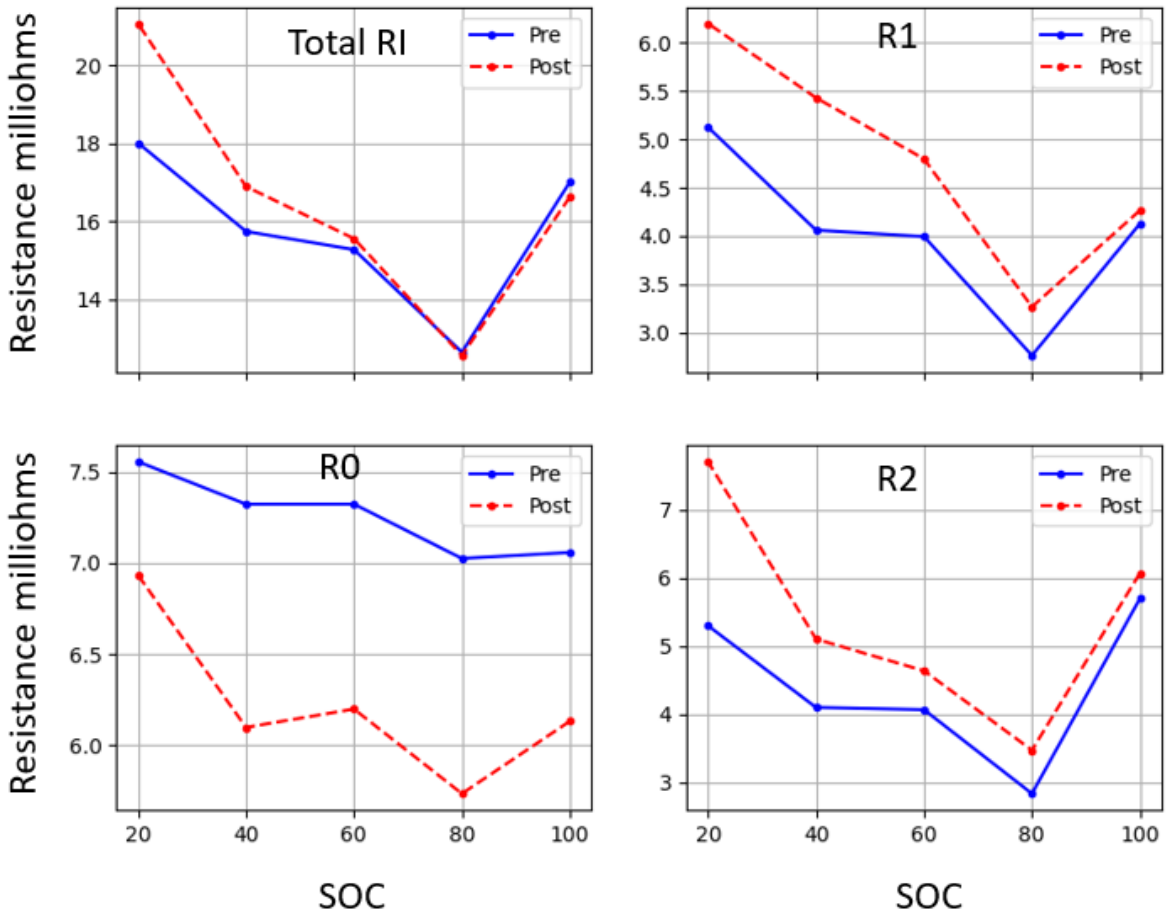

Figure 22: Internal resistance.

It is assumed that the refilling of DMC have changed the composition of the solvent to be almost pure DMC. Pure DMC has lower conductivity than common solvent compositions like LP40 [34], so it would be expected for R0 to increase. A possible explanation for the reduction in R0 could be an ambient temperature difference during the HPPC [5]. However, the observed average surface temperature during the HPPC before and after implementation was 25.1 and 25.9℃ which should not be enough to account for an average of 1 $m\Omega$ reduction. The change in R0 is therefore assumed to be unchanged within the accuracy of the HPPC test performed here.

R1, Which is dominated by the reaction resistance increased over the SOC range with the highest deviation at 40%SOC. It is expected that the implementation of capillaries might damage some of the electrode surface area where the capillaries are, and possibly other areas as a result of handling the electrodes during implementation. This

could result in new SEI layer formation and loss of lithium. In addition, some lithium salt may have been left on the original pouch. This could possibly lower the concentration of lithium enough to lower the equilibrium current density and increase the reaction overpotential [5].

For R2, which also increased, the concentration overpotential may have increased due to the same reasons as R1, lower concentration of lithium. In addition, if the solvent after implementation consists of mainly DMC, it is likely the viscosity have been increased [34]. This could effect the diffusivity of the electrolyte and increase the concentration overpotential [35].

The exact effect of the capillaries on the cell performance can not be easily detected by the measurements presented above. However, it is clear that the implementation procedure has affected the cell in a negative way through a resistance increase and capacity loss. It is likely that the main reason is the refilling with only DMC as solvent. It is possible, if the same as the original solvent composition was used and one could measure the amount of evaporated solvent, that the cell would be close to identical with the capillaries installed.

4.4 Temperature measurements and sensor performance

Cell 5 was cycled with a 0.5 C CCCV charge and CC discharge at 0.5, 1, 1.5 and 2 C. Fig. 23 show the voltage and current during the cycling, together with the corresponding temperatures from the three internal and three external FBGs. The notation used for an internal sensor is ”I” and external is ”E”. The three positions along the battery are denoted ”T” for tab end, ”M” for middle and ”B” for bottom end. Fig. 25 shows a 0.5C charge and 2C discharge cycle with only the EM and IM FBGs for clearer illustration. The FBGs showed a similar response as the external PT100 element, indicating that the capillaries successfully eliminated the strain contribution to the wavelength shift. At all the C-rates, the sharpest temperature rise occurs at discharge towards low SOC, which corresponds well with the highest Ri measured towards low SOC.

The 0.5 C charge curve in Fig. 25 shows a slowly increasing temperature with time up to approximately 50% SOC where the heat generation gets lower then the heat flux out of the cell for a short period before the heat generation increase again towards 100% SOC. The temperature variations are quite low with a temperature difference from low to high of approximately 1 ℃ for both internal and external signals. The shape of of the temperature curve fits well with the measured Ri which have a the lowest value at 80% SOC, as seen in Fig. 22. If one also considers the reversible heat contribution in Eq. 1, the middle temperature peak at approximately 50% SOC is expected. ΔS values for LFP cells from the literature [4], shown in Fig. 24, are positive from 30% SOC to 70% SOC, which corresponds well with the middle peak of the temperature signal. However, towards the end of the charge cycle, the internal temperature drops below the external temperature. This could be possible if the heat conduction trough the

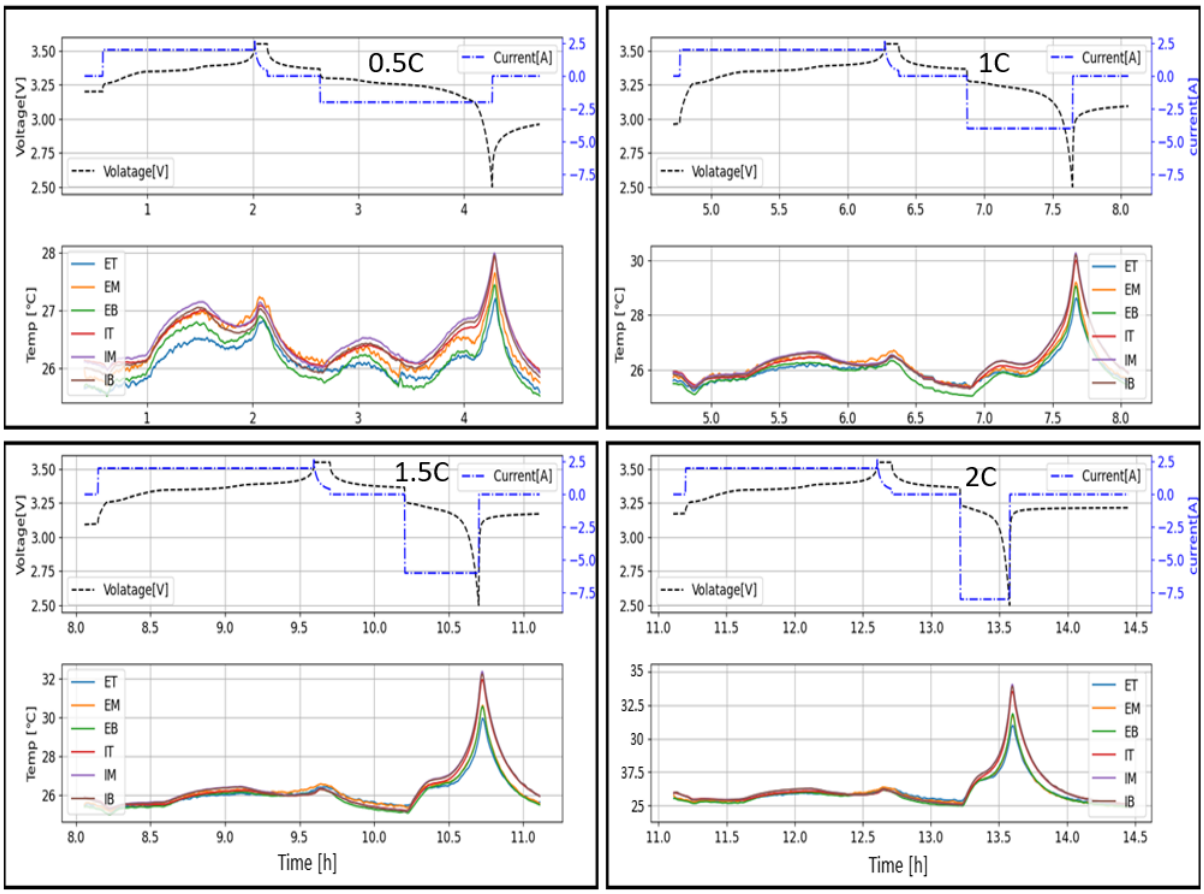

Figure 23: Temperature measurements at 1/2 C charge and 1/2, 1, 3/2 and 2 C discharge.

current collectors and tabs were greater the the heat convection from the pouch to air. However, as the temperature increase, the internal still stays below the external. This would indicate an uneven heat generation in the cross plane direction of the electrodes and higher heat generation closer to the pouch side where the external sensors are placed. Uneven heat generation can occur in LIBs [17], however, if this was the case, one would expect to observe higher external temperatures at different SOC and during discharging. Another possible explanation could be strain signal contribution. However, the glass capillaries encapsulating the FBG arrays should keep the strain contribution low and insignificant [36].

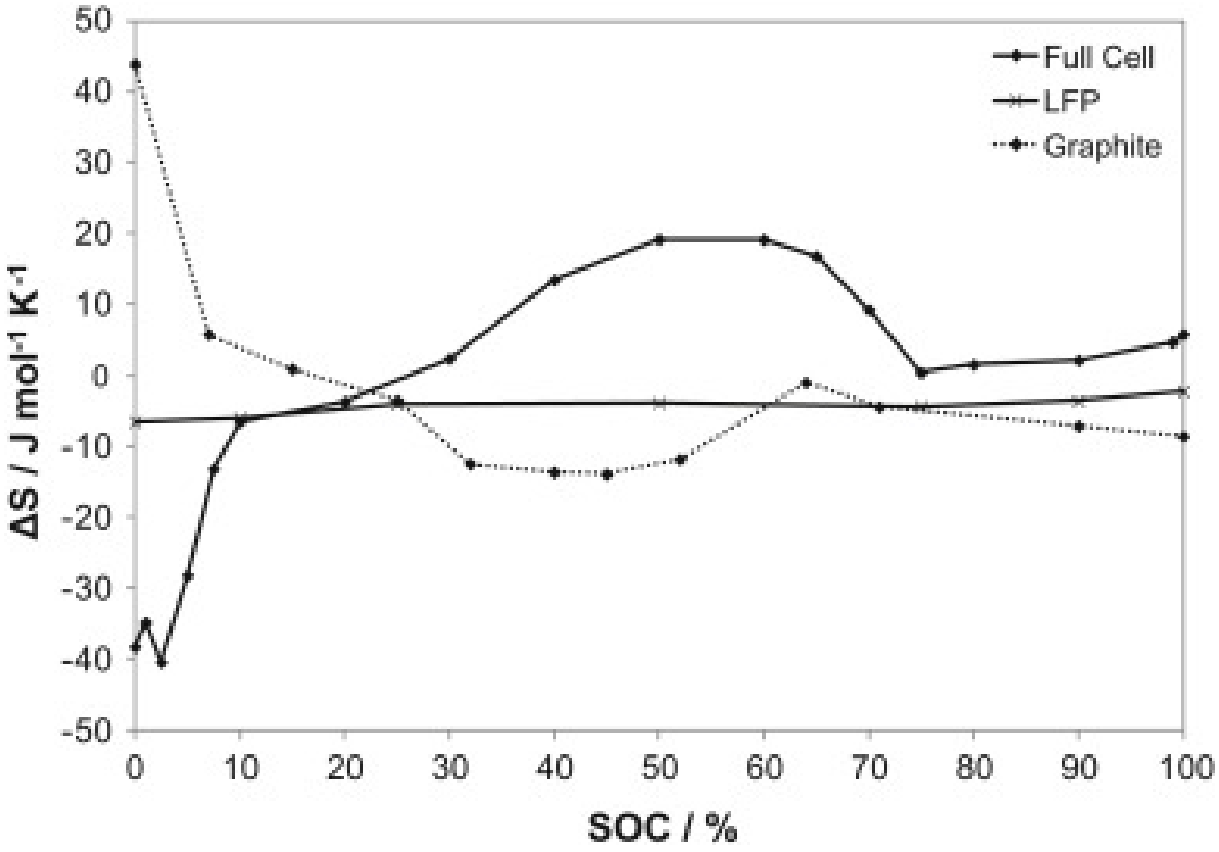

Figure 24: Δ S values of LFP cell [4].

All this considered, the most likely explanation would be the accuracy of the system. Even after the normalisation of the FBG signals the difference between the FBGs fluctuated with a value up to 0.1℃. So when it seems like the internal temperature is slightly below the external, they are instead equal. Improved accuracy could be obtained trough more reference points in the calibration or simply a spectrometer with higher accuracy and less drift.

In the discharge curve both the highest temperature and temperature difference between external and internal is at the end of discharge, towards 0% SOC. This as well corresponds well with the Ri values measured and the reversible heat of LFP cells. The highest Ri was measured at 20% and trending upwards toward 0% SOC. The entropy

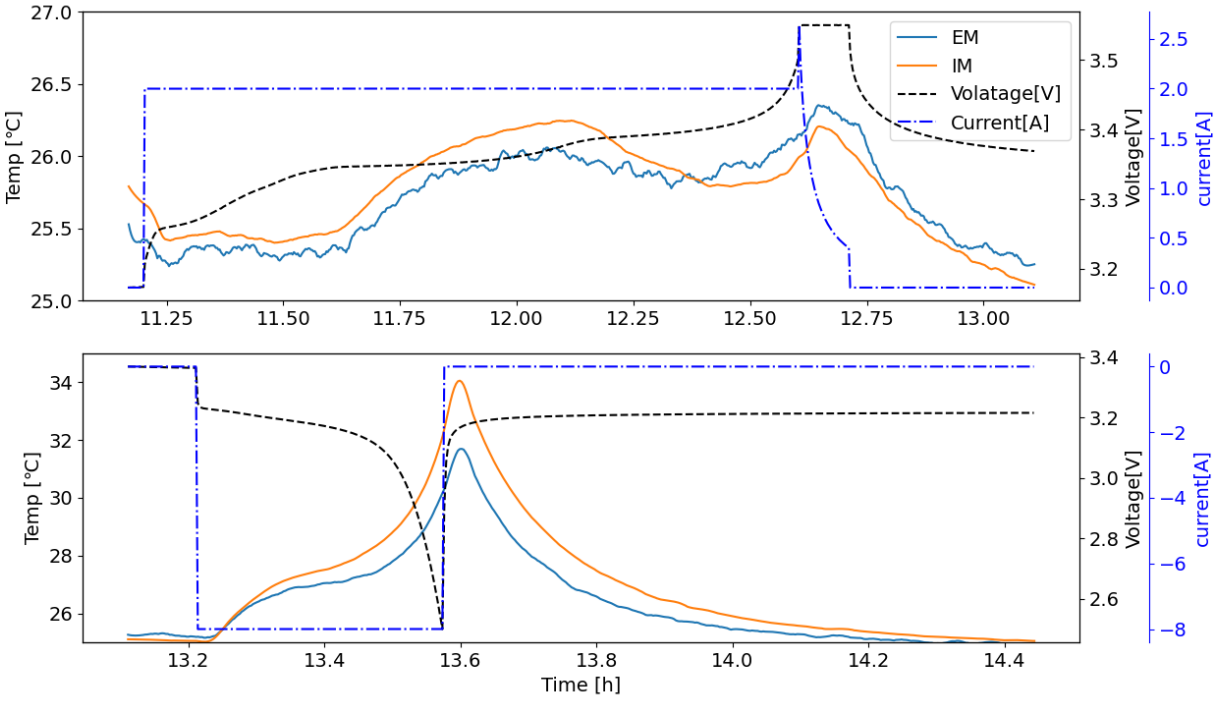

Figure 25: 1/2 C charge and 2 C discharge.

change values from literature [4] has its highest negative value towards 0% SOC and the negative value results in all the contributing elements in eq. 2 to be positive. The temperature difference was measured to be 2.75℃. This indicates the informational value of internal temperature measurements. Even at relative low C-rates of 2C, compared to the maximum allowed from the manufacturer at 35C, heat dos not dissipate immediately and internal temperature measurements can give key insight on cell behavior. In addition, a maximum Δ T of 2.75℃, further confirms the that strain have a low to no influence on the Bragg wavelength, as approximately the same Δ T values have been observed by others when using FBGs with no signal discrimination in cells with only 1 layer [11].

Fig. 26 shows the maximum temperature difference to ambient temperature during discharge at different C- rates and maximum temperature between internal and external FBGs at different C-rates. The internal temperatures increase more with C-rate then the external, indicating the cooling by convection to air and ambient temperature is not adequate to keep the internal temperature low at higher C-rates, as the trajectory of the internal and external curves are different. The internal temperature was similar at the middle an bottom of the cell and the temperature at the tab end was slightly lower. This could be due to in-plane cooling trough the current collectors and tabs [37]. This heat conduction effect is also visible at the external tab FBG, which is slightly lower then the middle and bottom. The temperature difference between internal and external sensors are shown in fig. 26 b. The different locations show varying temperature gradients with the steepest Δ T slope in the middle of the cell. This indicates that the temperature will

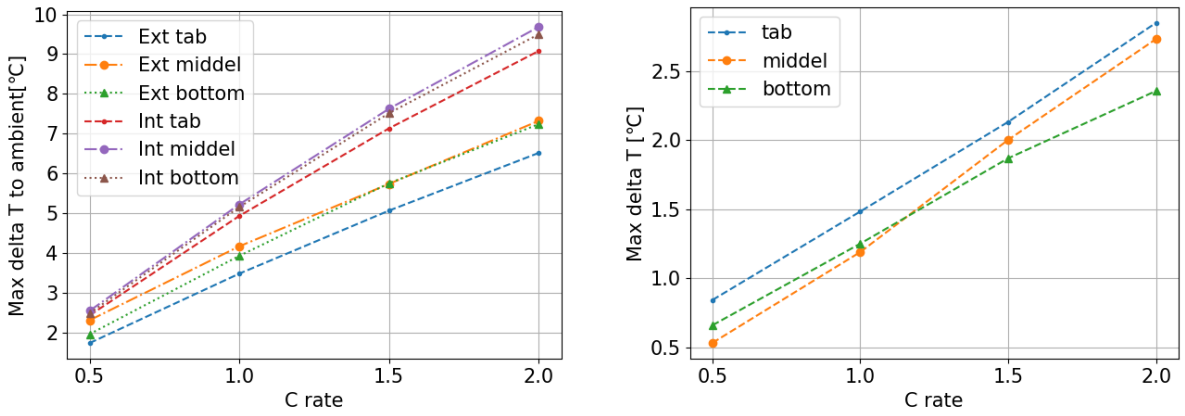

(a) (b)

Figure 26: a: Maximum delta T to ambient temperature at different C-rates. b: Maximum delta T between internal and external FBG

be highest in the middle of the cell at higher C-rates.

5 Conclusion and Future work

An attempt to embed FBG sensors into pre-fabricated LIB cells and measure internal temperature during cycling where made. Glass capillaries was used to eliminate the strain contribution to the reflected Bragg wavelength and a polypropylene bracket was used to protect the capillaries at the entry point of the cell. Furthermore, initial temperature measurements where made during cycling of the cell at different C-rates.

The polypropylene bracket successfully protected the capillaries at the entry point. However, due to the fragile nature of glass capillaries, the implementation procedure used here was unreliable as capillaries broke several times during the vacuum sealing of the cell. This might be solved by leaving a small area of the pouch open during the pressure sensitive sealing of the tab, and do the final sealing of the area left open at lower vacuum so the capillaries survive.

Using a pre-fabricated cell force the pouch to be replaced in order to implement the sensors. This resulted in evaporation of the electrolyte solvents and unfortunately the electrolyte composition was unknown so the cell was refilled with only DMC. This resulted in a 10% capacity drop and increasing of the total Ri of 7% at 40%SOC and 17% at 20% SOC. No apparent effect on the cell performance was found due to the capillaries. However, this might have been overshadowed by the effects from the solvent change.

The temperature measurements showed reasonable values and internal temperature

measurements in LIBs can clearly be advantageous when the internal temperature gradients are of interest. At 2 C discharge, a maximum temperature difference between external and internal of 2.75℃ was measured. Comparing this value to other studies done on with no signal discrimination indicates that the capillaries adequately isolated the FBGs from the strain contributions. However, the accuracy of the system limited the evaluation of temperature gradients to differences larger then ± 1℃. This can possibly be improved by other methods of calibration and signal processing.

Future work should be to improve on the issues mentioned above. If this is solved, the system could be used to monitor the evolution of heat generation while aging cells. In addition, thermal distribution and heat generation data at different working conditions could be used to improve thermal modeling of cells. Furthermore, the use of internal OF sensing as a part of BMS should be investigated. This wil raise a new set of challenges such as system cost, reliability and system integration into LIB production.

References

[1] Gregory L Plett. *Battery management systems, Volume I: Battery modeling*. Artech House, 2015.

[2] Jacob J. Lamb, Bruno G Pollet, and Odne S. Burheim. Feasibility study report establishing giga factories for manufacturing of li-ion batteries in norway. 2019.

[3] Jacob J. Lamb, Odne S. Burheim, and Dag R. Hjelme. *Introduction*, pages 3–8. Springer International Publishing, Cham, 2020.

[4] Kirsi Jalkanen, T Aho, and K Vuorilehto. Entropy change effects on the thermal behavior of a lifepo4/graphite lithium-ion cell at different states of charge. *Journal of Power Sources*, 243:354–360, 2013.

[5] Odne Stokke Burheim. *Engineering energy storage*. Academic press, 2017.

[6] Center for Climate and Energy Solutions. Global manmade greenhouse gas emissions by sector, (accessed: 07.11.2020).

[7] Lena Spitthoff, Eilif S Øyre, Harald I Muri, Markus Wahl, Astrid F Gunnarshaug, Bruno G Pollet, Jacob J Lamb, and Odne S Burheim. Thermal management of lithium-ion batteries. In *Micro-Optics and Energy*, pages 183–194. Springer, 2020.

[8] Terrence Xu, Wei Wang, Mikhail L Gordin, Donghai Wang, and Daiwon Choi. Lithium-ion batteries for stationary energy storage. *Jom*, 62(9):24–30, 2010.

[9] Kailong Liu, Kang Li, Qiao Peng, and Cheng Zhang. A brief review on key technologies in the battery management system of electric vehicles. *Frontiers of mechanical engineering*, 14(1):47–64, 2019.

[10] Ajay Raghavan, Peter Kiesel, Lars Wilko Sommer, Julian Schwartz, Alexander Lochbaum, Alex Hegyi, Andreas Schuh, Kyle Arakaki, Bhaskar Saha, Anurag Ganguli, et al. Embedded fiber-optic sensing for accurate internal monitoring of cell state in advanced battery management systems part 1: Cell embedding method and performance. *Journal of Power Sources*, 341:466–473, 2017.

[11] Susana Novais, Micael Nascimento, Lorenzo Grande, Maria Fátima Domingues, Paulo Antunes, Nélia Alberto, Cátia Leitão, Ricardo Oliveira, Stephan Koch, Guk Tae Kim, et al. Internal and external temperature monitoring of a li-ion battery with fiber bragg grating sensors. *Sensors*, 16(9):1394, 2016.

[12] Euan McTurk, Tazdin Amietszajew, Joe Fleming, and Rohit Bhagat. Thermo-electrochemical instrumentation of cylindrical li-ion cells. *Journal of Power Sources*, 379:309–316, 2018.

[13] Aleksandra Fortier, Max Tsao, Nick D Williard, Yinjiao Xing, and Michael G Pecht. Preliminary study on integration of fiber optic bragg grating sensors in li-ion batteries and in situ strain and temperature monitoring of battery cells. *Energies*, 10(7):838, 2017.

[14] Chang-Jun Bae, Ashish Manandhar, Peter Kiesel, and Ajay Raghavan. Monitoring the strain evolution of lithium-ion battery electrodes using an optical fiber bragg grating sensor. *Energy technology*, 4(7):851–855, 2016.

[15] Micael Nascimento, Susana Novais, Markus S Ding, Marta S Ferreira, Stephan Koch, Stefano Passerini, and João L Pinto. Internal strain and temperature discrimination with optical fiber hybrid sensors in li-ion batteries. *Journal of Power Sources*, 410:1–9, 2019.

[16] Joe Fleming, Tazdin Amietszajew, Euan McTurk, David P Towers, Dave Greenwood, and Rohit Bhagat. Development and evaluation of in-situ instrumentation for cylindrical li-ion cells using fibre optic sensors. *HardwareX*, 3:100–109, 2018.

[17] Todd M Bandhauer, Srinivas Garimella, and Thomas F Fuller. A critical review of thermal issues in lithium-ion batteries. *Journal of the Electrochemical Society*, 158(3):R1, 2011.

[18] Masaki Yoshio, Ralph J Brodd, and Akiya Kozawa. *Lithium-ion batteries*, volume 1. Springer, 2009.

[19] Seong Jin An, Jianlin Li, Claus Daniel, Debasish Mohanty, Shrikant Nagpure, and David L Wood III. The state of understanding of the lithium-ion-battery graphite solid electrolyte interphase (sei) and its relationship to formation cycling. *Carbon*, 105:52–76, 2016.

[20] Naoki Nitta, Feixiang Wu, Jung Tae Lee, and Gleb Yushin. Li-ion battery materials: present and future. *Materials today*, 18(5):252–264, 2015.

[21] Heiner Heimes, Achim Kampker, Christoph Lienemann, Marc Locke, and Christian Offermanns. *LITHIUM-ION BATTERY CELL PRODUCTION PROCESS*. 02 2019.

[22] Lena Spitthoff, Jacob J. Lamb, Bruno G. Pollet, and Odne S. Burheim. *Lifetime Expectancy of Lithium-Ion Batteries*, pages 157–180. Springer International Publishing, Cham, 2020.

[23] Frank Richter, Signe Kjelstrup, Preben J.S. Vie, and Odne S. Burheim. Thermal conductivity and internal temperature profiles of li-ion secondary batteries. *Journal of Power Sources*, 359:592 – 600, 2017.

[24] Qingsong Wang, Ping Ping, Xuejuan Zhao, Guanquan Chu, Jinhua Sun, and Chunhua Chen. Thermal runaway caused fire and explosion of lithium ion battery. *Journal of power sources*, 208:210–224, 2012.

[25] Feng Leng, Cher Ming Tan, and Michael Pecht. Effect of temperature on the aging rate of li ion battery operating above room temperature. *Scientific reports*, 5:12967, 2015.

[26] Markus S. Wahl, Jacob J. Lamb, Harald I. Muri, Rolf K. Snilsberg, and Dag R. Hjelme. *Light Properties and Sensors*, pages 9–27. Springer International Publishing, Cham, 2020.

[27] Markus S. Wahl, Harald I. Muri, Rolf K. Snilsberg, Jacob J. Lamb, and Dag R. Hjelme. *Temperature and Humidity Measurements*, pages 31–43. Springer International Publishing, Cham, 2020.

[28] Alan D Kersey, Michael A Davis, Heather J Patrick, Michel LeBlanc, KP Koo, CG Askins, MA Putnam, and E Joseph Friebele. Fiber grating sensors. *Journal of lightwave technology*, 15(8):1442–1463, 1997.

[29] Frode Østby. Internal temperature measurements in lithium-ion batteries using fbg. 2020.

[30] Suguna Thanagasundram, Raghavendra Arunachala, Kamyar Makinejad, Tanja Teutsch, and Andreas Jossen. A cell level model for battery simulation. In *European Electric Vehicle Congress*, pages 1–13, 2012.

[31] Abraham Savitzky and Marcel JE Golay. Smoothing and differentiation of data by simplified least squares procedures. *Analytical chemistry*, 36(8):1627–1639, 1964.

[32] Zhansheng Guo, Yang Fan, and Shiyu Du. Influence of lithium hexafluorophosphate/ethylene carbonate/dimethyl carbonate electrolyte soaking on heat seal strength of polyamide 6/aluminum/cast-polypropylene laminates used as lithium-ion battery packaging. *Journal of Plastic Film & Sheeting*, 34(1):10–26, 2018.

[33] SW Lasoski Jr and Gerard Kraus. Polymer to metal adhesion. the system polyvinyl acetate–steel. *Journal of Polymer Science*, 18(89):359–376, 1955.

[34] Erik Björklund, Mara Göttlinger, Kristina Edström, Daniel Brandell, and Reza Younesi. Investigation of dimethyl carbonate and propylene carbonate mixtures for lini0. 6mn0. 2co0. 2o2-li4ti5o12 cells. *ChemElectroChem*, 6(13):3429–3436, 2019.

[35] Daniel J Noelle, Meng Wang, Anh V Le, Yang Shi, and Yu Qiao. Internal resistance and polarization dynamics of lithium-ion batteries upon internal shorting. *Applied energy*, 212:796–808, 2018.

[36] Kort Bremer, Elfed Lewis, Gabriel Leen, Brian Moss, Steffen Lochmann, and Ingo AR Mueller. Feedback stabilized interrogation technique for efpi/fbg hybrid fiber-optic pressure and temperature sensors. *IEEE Sensors Journal*, 12(1):133–138, 2011.

[37] Shovon Goutam, Alexandros Nikolian, Joris Jaguemont, Jelle Smekens, Noshin Omar, Peter Van Dan Bossche, and Joeri Van Mierlo. Three-dimensional electro-thermal model of li-ion pouch cell: Analysis and comparison of cell design factors and model assumptions. *Applied thermal engineering*, 126:796–808, 2017.

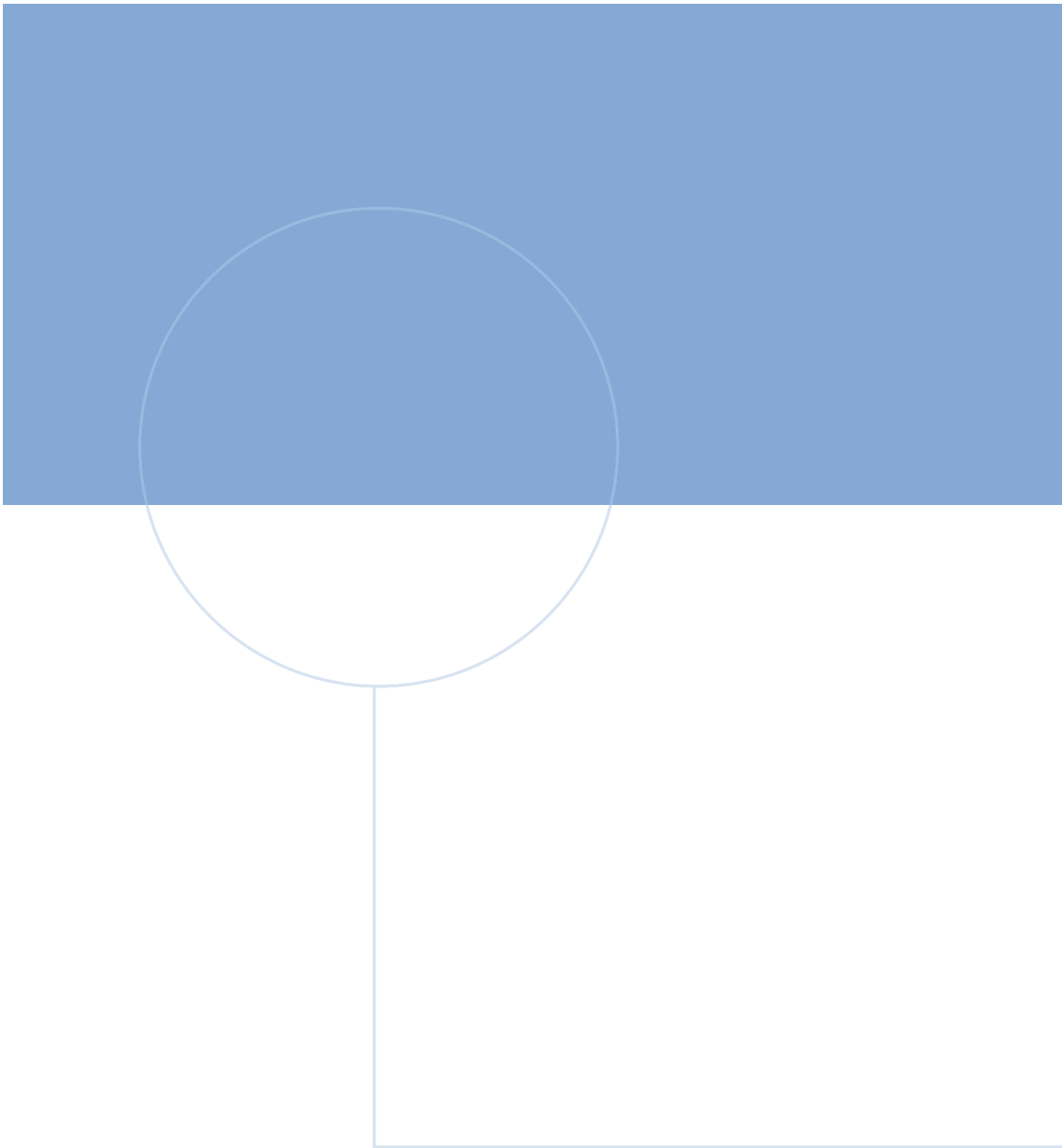

NTNU

Kunnskap for en bedre verden